J. Fluid Mech. (2005), *vol.* 545, *pp.* 67–111.
doi:10.1017/S0022112005006889 Printed in the United Kingdom

Fully resolved simulations of particle–turbulence interaction

By TRISTAN M. BURTON[1] AND JOHN K. EATON[2]

[1]Mechanical Engineering Department, US Naval Academy, Annapolis, MD 21402, USA
[2]Mechanical Engineering Department, Stanford University, Stanford, CA 94305, USA

(Received 5 November 2004 and in revised form 6 June 2005)

The interaction between a fixed particle and decaying homogeneous isotropic turbulence is studied numerically using an overset grid that provides resolution of all scales of fluid motion. A description of the numerical technique and validation of the solution procedure are presented. An ensemble of 64 simulations with the particle in different regions of the flow is computed. The particle diameter in the simulations is approximately twice the size of the unladen Kolmogorov length scale, and the maximum value of the particle Reynolds numbers due to the turbulent fluctuations is close to 20. Ensemble averages of quantities from the numerical solutions are used to investigate the turbulence modification and the fluid forces on the particle. Volume-averaged profiles of the turbulent kinetic energy and dissipation rate from the overset grid simulations reveal that the displacement of fluid by the particle and the formation of the boundary layer at the particle surface lead to turbulence modification in a local region. Time histories of the force applied to the particle from each overset grid simulation are compared to those predicted by a particle equation of motion. The particle equation of motion is shown to underpredict the root mean square (RMS) force applied to the particle by the turbulence. RMS errors between the forces from the overset grid simulation and those predicted by the particle equation of motion are shown to be between 15 % and 30 % of the RMS force on the particle. The steady viscous drag force is shown to be the dominant term in the particle equation of motion while the history integral term is negligible.

1. Introduction

Particle, droplet and bubble laden flows are ubiquitous in nature. Examples include dust storms, volcanic ash eruptions, rain, snowflake and meteorite formation, and the transport of blood corpuscles in the human body. The study of this portion of the broader field of multiphase flows has received a great deal of attention owing to the wide variety of engineering applications where particles, droplets and bubbles interact with a fluid carrier phase. Coal combustors, solid-fuel rocket engines, pneumatic conveyers and spray combustors are all engineering devices whose performance can be enhanced by a detailed understanding of the interaction between the dispersed and carrier phases.

A number of complicated phenomena occur in particle-laden flow systems. Depending on their inertia, particles can preferentially concentrate into carrier flow regions with low vorticity and high strain rate. This behaviour can lead to local concentrations of particles that far exceed the mean concentration. Particle-laden flow systems with a sufficient mass loading of particles can show turbulence levels

that are significantly reduced from their unladen values. However, other systems show that turbulence levels are increased by the presence of particles. In cases where the interparticle separation is small, particle collisions and hydrodynamic interactions play an important role in determining the overall system behaviour. Each of these phenomena help to highlight the fact that a particle-laden flow system is always more complicated than its single-phase counterpart owing to a broader range of length and time scales and the increased number of parameters introduced by the presence of a dispersed phase. It is also apparent that momentum coupling between the discrete and carrier phases plays a key role in the behaviour of particle-laden flow systems.

The complexity of the momentum coupling in a particle-laden flow depends on a number of parameters. The particle volume fraction, α_p, particle mass loading, ϕ_p, and the ratio of the particle time constant, τ_p, to the Kolmogorov fluid time scale, τ_k, given by the Stokes number, St, determine the type of momentum coupling that will occur. In systems where the particle diameter, d_p, is small and the ratio of the fluid density, ρ, to the particle density, ρ_p, is small, α_p can be small while ϕ_p is non-negligible and $St \simeq O(10)$. In this regime, the system is two-way coupled as the carrier flow disperses the particulate phase and the particulate phase modifies the carrier flow, but particle–particle interactions are negligible.

1.1. *Turbulence modification in experiments*

A large number of experimental studies have focused on turbulence modification in two-way-coupled particle-laden flows. Kulick, Fessler & Eaton (1994) and Paris & Eaton (2001) found that glass and copper particles significantly reduced the turbulence at the centreplane of a vertical fully developed air channel flow. However, measurements by Sato & Hishida (1996) in a similar geometry with glass particles and water as the carrier fluid showed augmentation of the streamwise turbulence intensity in the core region of the channel. Fessler & Eaton (1999) measured the effect of particles in a backward-facing step flow and found that turbulence levels at locations above the step height were reduced by up to 35 % for a 40 % mass loading of 150 μm glass particles. The turbulence in the particle-laden vertical air pipe flow studied by Tsuji, Morikawa & Shiomi (1984) was attenuated by 200 μm plastic particles but augmented by 3 mm plastic particles. Measurements of a vertical flat-plate turbulent boundary layer in air by Rogers & Eaton (1991) showed that a 20 % mass loading of 70 μm copper particles reduced the streamwise turbulence intensity by up to 35 %. Parthasarathy & Chan (2001) performed turbulence measurements in a water jet laden with 64 and 180 μm glass beads. Their results showed that the radial velocity fluctuations were reduced up to 30 % by the large particles while the axial velocity fluctuations were unchanged.

The brief review of experimental work in the previous paragraph shows that turbulence modification by particles is an extremely complex phenomenon. Attempts have been made to determine a reduced parameter set with which to classify the results from the many different types of experiment. Gore & Crowe (1989) compiled data from the centreline of a large number of particle-laden jet and pipe experiments and showed that the ratio of d_p to the characteristic length of the most energetic eddies of the carrier flow could be used to determine the type of turbulence modification. Hetsroni (1989) suggested that the particle Reynolds number based on the slip velocity and the particle diameter, Re_p, determines the nature of the turbulence modification by particles. Elghobashi (1994) presented a slightly more complicated classification map where St and α_p can be used to determine if turbulence augmentation or attenuation occurs.

While d_p, α_p, Re_p and St affect the behaviour of two-way-coupled particle-laden flow systems, it is clear from a review of the experimental literature that turbulence modification is controlled by an even larger number of parameters. Simplified classifications may be used in specific flow configurations to make an initial assessment of the possibility of turbulence modification, but no information can be gained as to the degree of turbulence attenuation or augmentation. In order to develop the predictive capability required to improve engineering devices, a more detailed understanding of the physics of particle–turbulence interaction is required. This understanding can be facilitated through the use of numerical simulations which, although restricted to lower Reynolds numbers than experiments, can provide detailed information that cannot be accurately measured in experiments.

1.2. *Resolved simulations*

Fully resolved simulation of particle-laden flow systems is a challenging task. The procedure requires the solution of the unsteady incompressible Navier–Stokes equations in a complex domain that changes in time as the particles move through the carrier fluid. The computation must resolve the effect of the no-slip boundary condition at each particle surface in order to predict accurately the motion of the particles and the resulting turbulence modification. In spite of the computational expense, several techniques have been developed to solve the coupled equations of fluid and particle motion with resolution of the no-slip boundary condition at the particle surface. This group of computational procedures includes the arbitrary Lagrangian–Eulerian (ALE) technique (see Hu, Patankar & Zhu 2001) which has been used primarily for two-dimensional simulations, and the deformable-spatial-domain/stabilized space–time (DSD/SST) technique which was applied to the three-dimensional direct numerical simulation (DNS) of 1000 spheres falling in a liquid tube by Johnson & Tezduyar (1999).

A number of less-expensive numerical procedures suitable for simulating particle–fluid interaction have been developed and applied to particle-laden flows. These techniques avoid placing grid points on the surface of the particles and use a single uniform grid to capture the behaviour of both phases. Glowinski *et al.* (2001) describe a distributed Lagrange-multiplier (DLM) based fictitious domain methodology for the simulation of flows with moving boundaries that has been successfully applied to the simulation of the fluidization of a bed of 1204 spherical particles by Pan *et al.* (2002). The Physalis technique developed by Prosperetti & Oğuz (2001) was used to simulate 10 sedimenting cylinders by Zhang & Prosperetti (2003). An alternative technique for obtaining solutions to the equations of fluid mechanics is the lattice Boltzmann method (LBM) (see Chen & Doolen 1998). This method relies on simplified kinetic models that incorporate the microscopic behaviour of fluids, to produce averaged properties that obey the continuum equations. Simulations of the sedimentation of 32 000 solid particles using the LBM were performed by Ladd (1997). Feng & Michaelides (2004) developed an immersed-boundary LBM and simulated the sedimentation of 504 circular particles.

Advances in computational power and the development of numerical techniques with simplified representations of the interface between the phases have allowed fully or partially resolved simulations of thousands of particles in simple flows. However, these simulations lack the complexity of turbulent flow and the number of particles is still orders of magnitude below those found in industrial and experimental particle-laden flows. In order to make simulation of these flows computationally tractable, the requirement of resolution of the flow around each particle must be relaxed.

Without resolution of the flow, the forces and torques at the particle surface cannot be directly computed. Therefore, an alternative means must be used to incorporate the momentum coupling between the phases. Typically, a Lagrangian particle equation of motion is used to move the particles through the flow domain and a force coupling scheme is used to account for modification of the carrier phase.

1.3. *Particle equation of motion*

Much of the history of the equation of motion for a spherical particle in a turbulent carrier fluid is described by Maxey & Riley (1983). They rederived the equation of motion from first principles and included the effects of spatial variations in the carrier phase velocity. The derivation assumes that the particle is small compared to the length scale of the variations in the undisturbed flow, the strain rate is small, and that Re_p is small. These restrictions limit the applicability of the Maxey–Riley particle equation of motion, and a large amount of numerical work has been done in an attempt to validate and/or correct the terms in the equation to develop a modified equation for particle-laden flows with larger Re_p (see Michaelides 2003). A suitable general form for the particle equation of motion at moderate Re_p is given by Bagchi & Balachandar (2003*b*),

$$m_p \frac{\mathrm{d}\boldsymbol{V}}{\mathrm{d}t} = \boldsymbol{F}_d + 3\pi\mu d_p \int_{-\infty}^{t} K(t-\tau,\tau)\left(\frac{\mathrm{d}\boldsymbol{u}}{\mathrm{d}\tau} - \frac{\mathrm{d}\boldsymbol{V}}{\mathrm{d}\tau}\right)\mathrm{d}\tau + C_M m_f \left(\frac{\mathrm{D}\boldsymbol{u}}{\mathrm{D}t} - \frac{\mathrm{d}\boldsymbol{V}}{\mathrm{d}t}\right) + m_f \frac{\mathrm{D}\boldsymbol{u}}{\mathrm{D}t} + (m_p - m_f)\boldsymbol{g}, \tag{1.1}$$

where m_p is the mass of the particle, μ is the fluid viscosity, m_f is the mass of fluid displaced by the particle, $\boldsymbol{u}$ is the fluid velocity undisturbed by the presence of the particle, $\boldsymbol{V}$ is the particle velocity, $\mathrm{D}/\mathrm{D}t = \partial/\partial t + \boldsymbol{u}\cdot\nabla$ is the total derivative following a local fluid element, $\mathrm{d}/\mathrm{d}t = \partial/\partial t + \boldsymbol{V}\cdot\nabla$ is the total derivative following the particle, and all the undisturbed fluid terms are evaluated at the location of the particle centre.

The first term on the right-hand side of (1.1) is the steady viscous drag force. Typically, a drag correlation based on a fit to experimental and simulation data is used to specify $\boldsymbol{F}_d$. The most common correlation used for particle-laden flows is that of Schiller and Nauman (see Clift, Grace & Weber 1978) which is valid for $Re_p < 800$. Using this correlation, the steady viscous force can be expressed as

$$\boldsymbol{F}_d = 3\pi\mu d_p(\boldsymbol{u} - \boldsymbol{V})\left[1 + 0.15Re_p^{0.687}\right]. \tag{1.2}$$

However, (1.2) ignores the effect of the strain rate, $\nabla\boldsymbol{u}$, on $\boldsymbol{F}_d$. Bagchi & Balachandar (2003*b*) used simulation results for steady axisymmetric (Magnaudet, Rivero & Fabre 1995) and planar straining flows (Bagchi & Balachandar 2002*c*) past a sphere to show that there is a complex dependence of $\boldsymbol{F}_d$ on strain. Because of the complexity of the dependence for simple straining flows and the lack of a corresponding expression for a turbulent flow, (1.2) will continue to be used for simulation of particle-laden turbulent flows.

The second term is the history force which accounts for increased viscous drag due to unsteadiness. Analytical formulae for the history kernel, $K(t-\tau,\tau)$, at moderate Re_p in a uniform ambient flow have been proposed by Mei & Adrian (1992) and Kim, Elghobashi & Sirignano (1998). In both cases, the history kernel goes as $(t-\tau)^{-1/2}$ at short times and $(t-\tau)^{-2}$ at longer times. The results of Bagchi & Balachandar (2003*b*) indicate that the kernel of Mei & Adrian (1992) is inadequate for a particle

in a rapidly imposed straining flow. However, Bagchi & Balachandar (2003*b*) and Kim *et al.* (1998) show that the history force is not significant in simulations of freely translating particles.

The third term is the added mass force which is the force required to accelerate the fluid that is displaced by the sphere. In the potential and creeping-flow regimes, the added mass coefficient, C_M, is known to be 1/2. A number of numerical studies have shown that the form of the added mass term in (1.1) with $C_M = 1/2$ is correct for a particle in a viscous fluid at moderate Re_p (Mei, Lawrence & Adrian 1991; Chang & Maxey 1995; Magnaudet, Rivero & Fabre 1995; Bagchi & Balachandar 2003*b*). The remaining terms on the right-hand side of (1.1) are the force due to the pressure gradient and viscous stresses in the undisturbed fluid and the force due to gravity.

In addition to the forces on the right-hand side of (1.1), particles may also experience lift forces due to shear (see Saffman 1965; McLaughlin 1991) and particle rotation (see Rubinow & Keller 1961). The forms of the terms representing these forces were derived analytically under the assumption of small Re_p. The lift forces for particles at moderate Re_p are usually assumed to be smaller than the drag force in the same direction, and are neglected. In cases where d_p is of the same order as the length scale of the flow variations, the Faxén corrections due to the curvature of the undisturbed velocity field are required to predict accurately the forces on the particle. The form of the Faxén corrections can be derived analytically in the low Re_p limit (see Maxey & Riley 1983). However, a suitable form for the Faxén corrections at moderate Re_p has not yet been developed.

1.4. *Force coupling*

Equation (1.1) provides a way to calculate the motion of a particle without resolving the flow to the particle surface. In unresolved simulations of two-way coupled flows, forces from the particles must be applied onto the carrier phase to introduce modification of the carrier phase. Therefore, an additional term is added to the right-hand side of the Navier–Stokes equations. One way to specify this forcing term is to assume that each particle applies a point force with the same magnitude as the force applied to the particle by the fluid, but in the opposite direction. The total force applied to each fluid grid node during the solution procedure is a weighted combination of the point forces from particles inside a specified local region. This technique is called the point-force approximation.

In addition to the point-force approximation, there are other numerical techniques for applying the effect of the particle onto the carrier phase. A modified point-force technique that replaces the point forces on the right-hand side of the Navier–Stokes equation using the pressure gradient and stress tensor terms from an analytical velocity disturbance field was proposed by Pan & Banerjee (1996). A novel force-coupling technique that obviates the solution of the particle equation of motion was developed by Maxey *et al.* (1997). The technique uses a Gaussian distribution of the force from the particle onto the fluid. The particle velocity is obtained by filtering the fluid velocity field. Further development and validation in sedimenting flows has been done by Maxey & Patel (2001) and Lomholt, Stenum & Maxey (2002).

1.5. *Unresolved turbulent simulations*

Fully resolved simulations of simple flows with a limited number of particles are computationally expensive. Simulations of turbulent flow are also computationally

expensive owing to the wide range of scales that must be resolved even in the absence of a particulate phase. Therefore, simulations of two-way-coupled particle-laden turbulent flows use force-coupling techniques and the particle equation of motion.

Spectral simulations of particle-laden stationary isotropic turbulent flow have been performed by Squires & Eaton (1990*a*) and Boivin, Simonin & Squires (1998) using point-force coupling. Particles were found to reduce the equilibrium turbulent kinetic energy and dissipation rate with increasing mass loading. Elghobashi & Truesdell (1993) used finite-difference techniques and point-force coupling to simulate the interaction between decaying homogeneous isotropic turbulence and small solid particles. Their results show an increased decay of turbulent kinetic energy and slower decay of the dissipation rate at short times, compared to the unladen case. A similar numerical method was used by Druzhinin (2001) to simulate modification of decaying turbulence by microparticles ($\tau_p \ll \tau_k$). Two-way-coupled point-force spectral simulations of decaying homogenous isotropic turbulence were performed by Sundaram & Collins (1999). Similar trends to those seen by Elghobashi & Truesdell (1993) were observed in the time histories of the fluid kinetic energy and dissipation rate.

Rouson, Eaton & Abrahamson (1997) performed a spectral DNS of particle–turbulence interaction in a fully developed turbulent channel flow using point-force coupling. The particles were the same as those used in the experiments of Kulick *et al.* (1993), but the Reynolds number of the simulated flow was only a quarter of the experimental value. Rouson *et al.* (1997) found no significant turbulence modification by a 20 % mass loading of copper particles, casting doubt on the ability of the point-force approximation to predict turbulence modification accurately. A similar spectral simulation of particle-laden turbulent channel flow including the effect of collisions was done by Li *et al.* (2001). The wall-normal and spanwise fluid velocity fluctuations in the simulations were reduced by the particles, leading to greater anisotropy in the turbulence in agreement with the results of Rouson *et al.* (1997).

Maxey *et al.* (1997) performed spectral simulations of particles under the influence of gravity in forced and decaying homogeneous isotropic turbulence using the Gaussian force distribution technique. At high wavenumbers, the forced turbulence simulations showed that the effect of the particle force on the energy budget was small compared to the nonlinear transfer. In the decaying turbulence simulations, the two effects were of similar magnitude. Pan & Banerjee (1996) simulated the effects of near-neutral density solid particles on turbulent flow in a horizontal open channel using spectral methods and the modified point-force technique. Particles smaller than the Kolmogorov length scale in the near-wall region were found to suppress turbulence, whereas larger particles enhanced the turbulence.

1.6. *Objectives and approach*

A review of the turbulent particle-laden-flow literature shows that the interaction between particles and turbulence is complex and that the understanding of the turbulence modification process is limited at best. While experiments and unresolved simulations provide a large amount of information that is useful in assessing the impact of particles on a variety of turbulent flows, neither approach provides the accuracy required to enable the general prediction of turbulence modification. Predictive capability will only come from a detailed understanding of the physics of particle–turbulence interaction.

There have been a large number of fully resolved simulations investigating laminar flow over fixed particles (see Mei *et al.* 1991; Kim *et al.* 1993, 1995, 1997; Chang & Maxey 1994, 1995; Magnaudet *et al.* 1995; Ghidersa & Dušek 2000; Mittal 2000; Tomboulides & Orszag 2000; Bagchi & Balachandar 2002 *a–c*), particles undergoing prescribed motion (see Mei 1994), and freely moving particles (see Kim *et al.* 1998; Bagchi & Balachandar 2002*a*, 2003*b*). However, there are few simulations of fully resolved turbulent flow over particles. Bagchi & Balachandar have performed high-accuracy spectral simulations of turbulent flow past a fixed particle (2003*a*, 2004) by sweeping a frozen isotropic turbulent field past the particle. The use of the frozen isotropic turbulent field as an inflow boundary condition prevented the particle from modifying the inflow turbulence. Therefore, this numerical technique is suitable only for the cases with non-zero mean slip velocity that were considered by the authors.

In this work, the fully coupled interaction between a fixed particle and a turbulent flow with zero mean slip velocity is considered. We perform a series of simulations of decaying homogeneous isotropic turbulence with a fixed particle, and the results are used to analyse turbulence modification in the region near the particle and the force applied to the particle by the turbulent field. The use of a fixed particle could be justified as relevant to turbulence modification by heavy particles moving at the mean flow velocity in decaying turbulence behind a grid or particles in microgravity. However, these simulations are directed more toward developing an understanding of the fundamental physics than a specific turbulent particle-laden flow. Therefore, the results of the simulations will be useful in directing the development of modelling techniques for unresolved simulations of turbulent particle-laden flows of interest in engineering applications.

2. Numerical method

Accurate simulation of turbulent flow around a fixed particle requires resolution of a range of scales from the large turbulent eddies to the boundary layer at the particle surface. In order to capture this range of scales, we use an overset grid composed of a Cartesian background grid and a body-fitted spherical grid. The Cartesian grid is sized to capture the range of turbulent scales in the absence of the particle and the spherical grid provides the extra resolution required to capture the effects of the no-slip boundary condition at the particle surface. Information is transferred to the pseudoboundary nodes at the outer radial boundary of the spherical grid from the Cartesian grid via interpolation. A large portion of the Cartesian grid underneath the spherical grid is designated as a hole region since the spherical grid provides the solution in that region. Information is transferred from the spherical grid to the Cartesian grid pseudoboundary nodes at the edge of the hole region via interpolation. With the solution of the incompressible Navier–Stokes equations on each grid and the transfer of information in both directions between the grids via interpolation, a fully coupled solution of the governing equations is obtained.

2.1. *Governing equations*

For an incompressible flow, the non-dimensional Navier–Stokes and continuity equations can be written as

$$\frac{\partial \boldsymbol{u}}{\partial t} = \nabla \cdot f - \nabla p, \tag{2.1a}$$

$$0 = \nabla \cdot \boldsymbol{u}, \tag{2.1b}$$

where $\boldsymbol{u}$ is the fluid velocity vector, p is the pressure, and f is the combined viscous stress and nonlinear term tensor. For solution on the Cartesian grid, (2.1a)–(2.1b) are written using Cartesian coordinates and the Cartesian velocity vector, (u, v, w), where u, v and w are the velocity components in the x, y, and z directions, respectively. For solution on the spherical grid, (2.1a)–(2.1b) are written using spherical coordinates and the spherical velocity vector, (u_r, u_θ, u_ϕ), where u_r, u_θ and u_ϕ are the velocity components in the radial, tangential ($0 \leqslant \theta \leqslant \pi$) and azimuthal ($0 \leqslant \phi \leqslant 2\pi$) directions, respectively.

The variables in (2.1a)–(2.1b) are non-dimensionalized by the particle diameter, d_p, and the initial root mean square (RMS) velocity fluctuation, u_{rms_0}. The non-dimensional variables are defined as

$$(x, y, z, r) = \frac{(x^*, y^*, z^*, r^*)}{d_p}, \qquad t = \frac{t^* u_{rms_0}}{d_p}, \tag{2.2a}$$

$$(u, v, w, u_r, u_\theta, u_\phi) = \frac{(u^*, v^*, w^*, u_r^*, u_\theta^*, u_\phi^*)}{u_{rms_0}}, \qquad p = \frac{p^*}{\rho u_{rms_0}^2}, \tag{2.2b}$$

$$Re = \frac{u_{rms_0} d_p}{\nu}, \tag{2.2c}$$

where the superscript * denotes a dimensional quantity and ν is the fluid kinematic viscosity. All results in this work are reported in terms of non-dimensional variables based on d_p and u_{rms_0} unless otherwise indicated.

2.2. *Geometry and grid*

The governing equations are solved using an overset grid composed of a uniform Cartesian grid with $N_x \times N_y \times N_z = 192 \times 192 \times 192$ points and a spherical grid with constant geometric stretching in the radial direction and $N_\phi \times N_r \times N_\theta = 192 \times 192 \times 96$ points. The Cartesian grid covers a cubic domain with sides of non-dimensional length, $L = 192$. The particle centre is located at $(x, y, z) = (95.5, 95.5, 95.5)$ and the spherical grid extends to a non-dimensional radius of 35 with the poles ($\theta = 0, \pi$) parallel to the Cartesian x-axis. A fixed overlap is specified such that all Cartesian cells with centres inside $r = 30.5$ are designated as hole nodes. A close-up of the overset grid near the particle surface is shown in figure 1 and a portion of the overlap region is shown in figure 2.

A staggered grid (Harlow & Welch 1965) arrangement of the dependent variables is used for the Cartesian and spherical grids. The locations of the velocity components and the cell-centred pressure nodes are shown in figure 3 for the Cartesian grid and figure 4 for the spherical grid. In both cases, the velocity components in all three directions are offset from the cell centre in the direction of the component. The i, j and k subscripts shown in figures 3 and 4 are used to reference locations in the x, y and z directions, respectively, and the ϕ, r and θ directions, respectively.

2.3. *Spatial discretization*

The appropriate forms of (2.1a)–(2.1b) are spatially discretized with second-order-accurate finite-volume flux differencing on each grid. The locations of the off-diagonal f tensor components required for this discretization are shown in figure 3 for the Cartesian grid and figure 4 for the spherical grid. The diagonal f tensor components required for the discretization are located at the cell centres with the pressure nodes in both coordinate systems. The discrete f tensor components at all locations are computed using second-order-accurate central differences and two-point

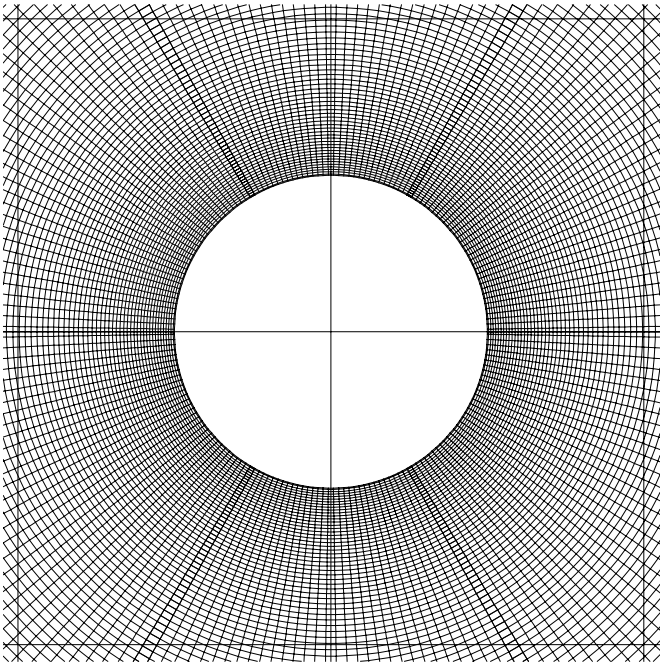

FIGURE 1. Close-up of overset grid near particle surface.

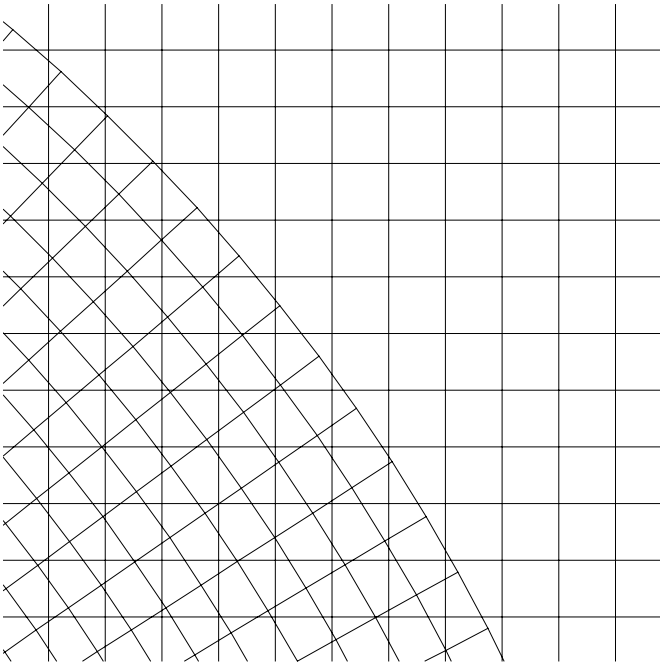

FIGURE 2. Close-up of overset grid overlap region.

averages. Details on the pole treatment and particle surface treatment used for spatial discretization of the governing equations in the spherical coordinate system can be found in the Appendix.

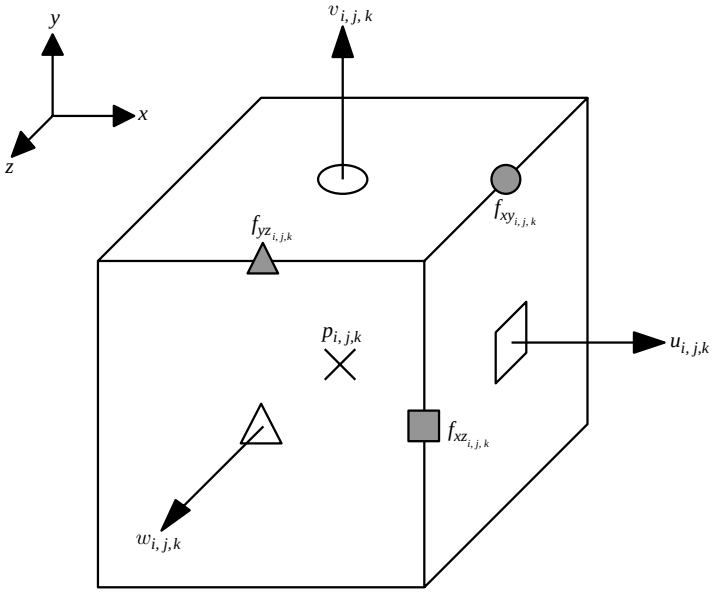

FIGURE 3. Cartesian staggered grid cell.

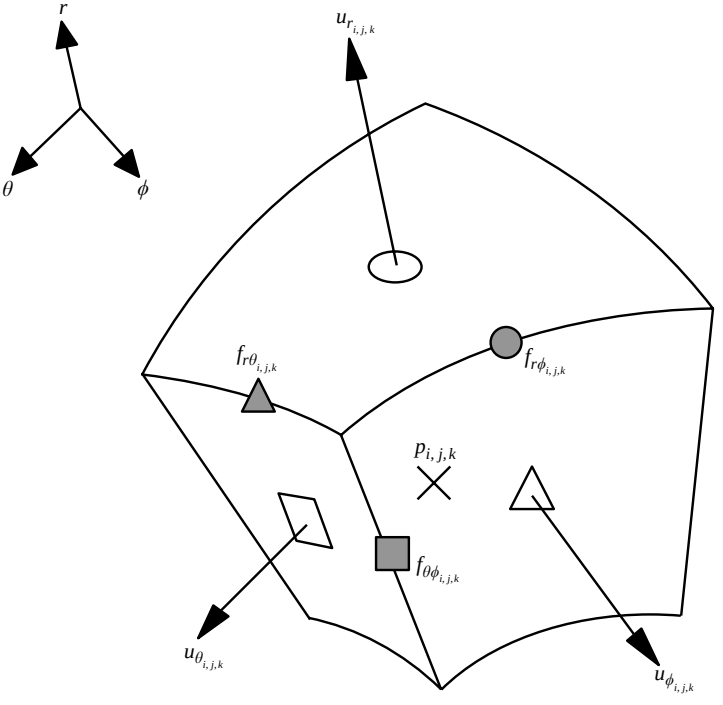

FIGURE 4. Spherical staggered grid cell.

2.4. *Temporal discretization*

The spatially discretized governing equations are integrated in time using the overset grid fractional-step method and the three-step time-advancement algorithm described

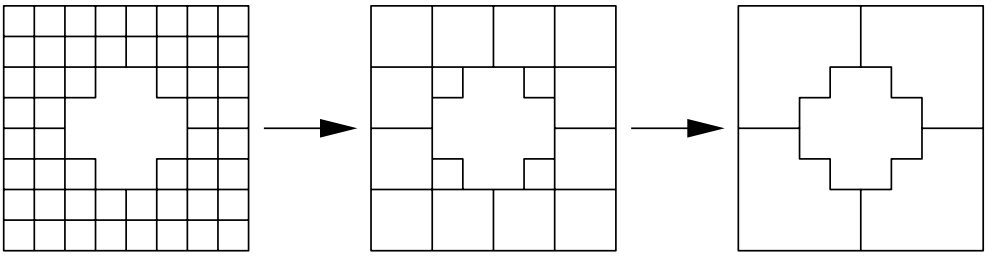

FIGURE 5. Cartesian multigrid coarsening process.

by Burton & Eaton (2002*a*). This numerical technique was used by Burton & Eaton (2002*b*) in two-dimensional simulations of fixed cylinders in a vortex array. The spatially discretized Cartesian grid momentum equations are time-advanced using explicit third-order Runge–Kutta for all velocity terms. The spatially discretized spherical grid momentum equations are time-advanced using implicit Crank–Nicolson for the radial and azimuthal viscous terms and the azimuthal convective terms, and explicit third-order Runge–Kutta for the remaining velocity terms. The pressure terms in the Cartesian and spherical grid momentum equations are time-advanced with implicit Euler. Further details on the hybrid time-advancement algorithm and the solution procedure for the fully discretized momentum equations can be found in Burton & Eaton (2003).

The momentum update and the enforcement of the continuity equation are performed in different steps in the fractional-step algorithm. The momentum update produces an intermediate velocity field which must then be projected to a divergence-free subspace. The Cartesian grid velocity field is first advanced since the update uses explicit time advancement. Once the intermediate Cartesian grid velocity field is determined, the pseudoboundary velocity values at the outer edge of the spherical grid can be interpolated and the discretized spherical grid momentum equations can be solved. After the intermediate velocity field is determined on the spherical grid, the velocity values at the pseudoboundary nodes on the Cartesian grid are determined by interpolation.

2.5. *Poisson equation*

The intermediate velocity field in the fractional-step algorithm is projected using the solution to the overset-grid discrete Poisson equation (see Burton & Eaton 2002*a*). The pressure is updated using the same solution. While the momentum updates on the two grids are effectively decoupled from one another, the solution to the discrete Poisson equation is fully coupled between the two grids. To solve the fully coupled problem, the iterative scheme described in Burton & Eaton (2002*a*) is used in combination with a multigrid method on each grid separately.

Geometric multigrid (see Briggs, Henson & McCormick 2000) is used to construct the equations for each multigrid level in the solution of the spherical-coordinate Poisson equation. Owing to the behaviour of the discrete operators near the poles of the spherical coordinate system, point relaxation is ineffective in the ϕ-direction (see Ruge *et al.* 2000). Therefore, line relaxation is used in the ϕ-direction. The multigrid method on the Cartesian grid is slightly more complicated owing to the hole region. The coarsening process on a two-dimensional grid with a hole in it is shown in figure 5. While the multigrid levels can be visualized in this way, it is not clear how to discretize the equation on the coarse grids owing to the irregular cell structure.

Therefore, an agglomeration multigrid technique is used to determine the coarse grid systems of equations (see Mavriplis & Venkatakrishnan 1995).

2.6. *Interpolation equations*

The velocities at the pseudoboundary nodes are obtained using third-order-accurate tri-quadratic interpolation of the velocity field on the other grid. The staggered grid arrangement of the dependent variables requires that all three components of the velocity vector on each grid are interpolated to the location of each component of the velocity vector on the other grid. Since the pseudoboundary velocities are interpolated directly to the staggered grid locations, the spatial differencing stencils near the outer boundary of the spherical grid and the hole boundary of the Cartesian grid need not be modified.

2.7. *Boundary and initial conditions*

Periodic boundary conditions are used at the boundary of the Cartesian grid for the turbulent simulations. In cases where the uniform flow over a sphere is simulated, the velocity at the inflow ($x = 0$) is set to the free-stream velocity and a convective boundary condition is used at the outflow ($x = L$). The no-slip boundary condition at the inner boundary of the spherical grid is applied directly to the u_r nodes since they are located on the particle surface. The effect of the no-slip boundary condition on the other velocity components is taken into account in the calculation of $f_{r\theta}$ and $f_{r\phi}$ at the particle surface discussed in the Appendix.

In order to simulate the interaction between a fixed particle and decaying turbulence, a turbulent field is first obtained on the Cartesian grid. This turbulent field is prescribed initially using the technique described by Lee (1985). The Fourier coefficients of the turbulent field are chosen to satisfy isotropy and continuity constraints and to produce a desired energy spectrum, $E(k)$,

$$E(k) = \frac{6}{\sqrt{\pi}} \frac{k^2}{k_p^3} \exp\left[-\left(\frac{k}{k_p} \right)^2 \right], \tag{2.3}$$

where k_p is the wavenumber at which $E(k)$ is maximum. The non-dimensional Kolmogorov length scale, η, and the Taylor microscale Reynolds number, Re_λ, are the input parameters used to specify k_p and the non-dimensional viscosity for the simulation, $1/Re$. The equations for Re and k_p can be derived from (2.3) and the definitions of the Kolmogorov length scale, the Taylor microscale in isotropic turbulence, and the dissipation rate (see Tennekes & Lumley 1974)

$$k_p = \left(\frac{20}{27 Re_\lambda^2 \eta^4} \right)^{1/4}, \tag{2.4}$$

$$Re = \sqrt{\frac{3}{10}} k_p Re_\lambda. \tag{2.5}$$

Once the Fourier coefficients have been generated, conjugate symmetry is enforced and an inverse Fourier transform is used to specify the velocity values at the staggered Cartesian grid locations. The velocity field satisfies (2.1*b*), but not its discretized version. Therefore, the velocity field is projected to a divergence-free subspace. This projection causes only minor changes to the velocity field.

The initial turbulent field satisfies the continuity and isotropy constraints and matches a desired analytical energy spectrum. However, higher-order statistics are not representative of real turbulence. Therefore, the turbulent simulation is first run

without a particle to develop a suitable initial point at which to insert the particle, and to compute turbulence statistics in the unladen flow. When the developed turbulent state is reached and the particle grid is introduced into the solution domain, fourth-order-accurate three-dimensional cubic splines are used to interpolate the velocity field to every node in the spherical coordinate system. The cubic spline interpolation does not guarantee that the velocity field interpolated to the spherical grid is divergence-free or that the velocity is zero at the particle surface. Therefore, the velocity field on both grids is projected (see Burton & Eaton 2002*a*) to produce a velocity field that satisfies the discrete continuity equation on both grids and has zero radial velocity at the particle surface.

2.8. *Solver validation*

2.8.1. *Spatial order of accuracy*

The Cartesian and spherical coordinate solvers were validated independently before they were combined to create the overset grid solver. Simulations of the Taylor vortex array were used to validate the spatial order of accuracy of the Cartesian coordinate solver. Since the solution is two-dimensional, one grid refinement study was done with the vortices in the (x, y)-plane and another study was done with the vortices in the (y, z)-plane. The simulations were run until the vortices had decayed to approximately half of their initial strength. Velocity and pressure RMS errors (see Burton & Eaton 2003) show that the non-zero velocity components and the pressure are second-order accurate in space and the error in the remaining velocity component is machine zero.

The spatial order of accuracy of the discretization used for the spherical coordinate solver was verified by calculating the force on a sphere due to uniform flow at $Re_\infty = 20$, where Re_∞ is the Reynolds number based on d_p and the free-stream velocity, U_∞. The force was calculated by numerically integrating the pressure and shear stress on the sphere surface. Uniform flow over a sphere at $Re_\infty < 210$ is steady and axisymmetric. Therefore, an axisymmetric version of the spherical coordinate code was used first to validate the spatial order of accuracy and to determine a grid-independent value for the drag coefficient,

$$C_d = \frac{F_d}{\frac{1}{2}\rho U_\infty^2(\pi/4)d_p^2}, \tag{2.6}$$

where all quantities on the right-hand side are dimensional and F_d is the drag force. The drag coefficient can be split into the pressure coefficient, C_p, which includes the part of the force due to the pressure, and the friction coefficient, C_f, which includes the part of the force due to the viscous stress.

The axisymmetric grid refinement studies were done in a domain that extended to $r = 25$. The velocity at the outer radial boundary was set to the free-stream velocity at the inflow, ($\pi/2 \leqslant \theta \leqslant \pi$), and calculated with a convective boundary condition at the outflow, ($0 \leqslant \theta < \pi/2$). The numerically computed values of C_f, C_p and C_d from the grid refinement study are presented in table 1. Each time the number of grid points was doubled, the radial stretching factor, $r_{stretch}$, was reduced so that the radial grid spacing adjacent to the sphere surface, Δr_1, was halved. If $r_{stretch}$ is not reduced during grid refinement, then the differencing in the radial direction will be first-order accurate. An estimate of the spatial order of accuracy of the code, h, can be obtained using a sequence of the numerically computed drag coefficient values (see Ferziger & Perić 1996)

$$h = \frac{\log\left[(C_{d2\Delta} - C_{d4\Delta})/(C_{d\Delta} - C_{d2\Delta})\right]}{\log 2}, \tag{2.7}$$

$N_r \times N_\theta$	$r_{stretch}$	Δr_1	C_f	C_p	C_d
64×32	1.07289	0.0200	1.738	1.062	2.801
128×64	1.03562	0.0100	1.710	1.031	2.742
256×128	1.01761	0.0050	1.703	1.023	2.726
512×256	1.00876	0.0025	1.702	1.021	2.722
Extrapolation			1.702	1.020	2.721

TABLE 1. Grid refinement study for axisymmetric simulation of uniform flow over a sphere at $Re_\infty = 20$.

Study	C_f	C_p	C_d
Dennis & Walker (1971)	1.708	1.024	2.730
Chang & Maxey (1994)	1.726	1.076	2.800
Magnaudet *et al.* (1995)	1.721	0.986	2.707
Kim *et al.* (1998)	1.725	1.038	2.763
Present study	1.702	1.021	2.722

TABLE 2. Force coefficients for uniform flow over a sphere at $Re_\infty = 20$.

where the grid spacing used to compute $C_{d\Delta}$ is a factor of two smaller than the grid spacing used to compute $C_{d2\Delta}$ and a factor of four smaller than that used to compute $C_{d4\Delta}$. Using the values of the drag coefficient from the 128×64, 256×128 and 512×256 simulations in (2.7) shows that the spherical coordinate solver is second-order accurate in space. Improved estimates of the force coefficients using Richardson extrapolation (see Ferziger & Perić 1996) are also presented in table 1. It is clear that the computed values on the 512×256 grid are very close to the grid-independent values as the Richardson extrapolation predicts little change with further grid refinement.

Several other authors have computed the force coefficients at $Re_\infty = 20$. A comparison of the results is presented in table 2. The ranges of variation are 1.4 %, 9.1 % and 3.4 % of the minimum value for C_f, C_p and C_d, respectively. None of the other studies in table 2 include a detailed grid refinement study at this Reynolds number and so it is difficult to account for the differences in the results. Streamlines and vorticity contours from the 512×256 grid solution reveal that the calculated flow is not separated at $Re_\infty = 20$, in agreement with the results of the other studies in table 2.

The effect of the boundary condition at the outer radial boundary was investigated by comparing the results in table 1 to similar calculations using the free-stream velocity along the entire outer radial boundary. It is well known that the use of Dirichlet boundary conditions at the outflow boundary will produce reflections that propagate back upstream into the flow domain. However, the reflections in our simulations remained far downstream and had a negligible effect on the force coefficients. These results indicate that our domain size was large enough to produce accurate calculations of the force coefficients and that Dirichlet boundary conditions may be used at this Re_∞ without adversely affecting the results.

The results from the axisymmetric grid refinement studies indicate that the discretizations of the spherical coordinate governing equations are second-order accurate in r and θ. Therefore, a grid refinement study in ϕ was required for the three-dimensional version of the spherical code. Since the azimuthal and tangential

$N_\phi \times N_r \times N_\theta$	$r_{stretch}$	Δr_1	C_f	C_p	C_d	Angle (deg.)
$32 \times 64 \times 16$	1.08758	0.01	1.863	1.128	2.991	0
$64 \times 64 \times 32$	1.08758	0.01	1.738	1.047	2.785	0
$128 \times 64 \times 64$	1.08758	0.01	1.708	1.027	2.735	0
$32 \times 64 \times 16$	1.08758	0.01	1.780	1.065	2.845	45
$64 \times 64 \times 32$	1.08758	0.01	1.718	1.032	2.749	45
$128 \times 64 \times 64$	1.08758	0.01	1.703	1.024	2.727	45
$32 \times 64 \times 16$	1.08758	0.01	1.805	1.081	2.887	90
$64 \times 64 \times 32$	1.08758	0.01	1.724	1.036	2.760	90
$128 \times 64 \times 64$	1.08758	0.01	1.704	1.025	2.729	90

TABLE 3. θ–ϕ grid refinement study for three-dimensional simulation of uniform flow over a sphere at $Re_\infty = 20$.

Grid	$r_{stretch}$	Δr_1	C_f	C_p	C_d
Overset	1.02509	0.0075	1.707	1.027	2.733
Spherical	1.02509	0.0075	1.705	1.026	2.731

TABLE 4. Force coefficients from overset grid simulation and spherical grid simulation of uniform flow over a sphere at $Re_\infty = 20$.

grid spacings should be the same to provide similar resolution in all directions, a θ–ϕ grid refinement study was performed instead. Three different angles of the uniform flow velocity to the poles of the spherical coordinate system were used as part of the grid refinement study, and the velocity at the outer radial boundary condition was set to the free-stream velocity. The calculated force coefficients are shown in table 3. Using (2.7), the three-dimensional code is shown to be second-order accurate in θ and ϕ, independent of the flow angle to the poles. Therefore, the spherical coordinate solver is second-order accurate in space for all coordinate directions.

The calculated values of the force coefficients in table 3 at the different flow angles are very similar on the $128 \times 64 \times 64$ grid. The range of variation is 0.29 % of the minimum value for all three coefficients. Therefore, the spherical coordinate solver produces results that are virtually independent of the flow angle to the pole. This is important for the turbulent simulations, as the flow angle to the poles is constantly changing in time.

Both Navier–Stokes solvers are second-order accurate in space. Therefore, the overset grid code composed of these two solvers will also be second-order accurate in space, provided that a fixed overlap is used during grid refinement and the interpolation is third-order accurate (see Burton & Eaton 2002*a*). A comparison of the force coefficients computed from a simulation using the overset grid described in § 2.2 and those computed from an axisymmetric simulation on a spherical grid with the same resolution in r and θ, is shown in table 4. The differences between the results of the two simulations are very small. The force coefficients from the overset grid solution are within 0.6 % of the values computed from the highest resolution axisymmetric simulation shown in table 1. Therefore, the overset grid system is capable of accurately resolving flows over the particle up to at least $Re_p = 20$.

2.9. *Temporal order of accuracy*

The temporal order of accuracy of each solver was validated independently. However, it is important also to validate the time accuracy of the overset grid code due to

the time-dependent corrections that are made to the discrete continuity equation as part of the fractional-step method (see Burton & Eaton 2002*a*) and the different time advancement algorithms on each component grid. One of the turbulent simulations was advanced for one time step, $\Delta t = 0.001$. Two other simulations starting from the same point were advanced for the same length of time with 10 and 100 time steps. Finally, an 'exact' solution was computed with 400 time steps. The errors in the calculated forces on the sphere when compared to the 'exact' solution demonstrated second-order time accuracy (see Burton & Eaton 2003). Therefore, the computed velocity components are second-order accurate in time as is expected owing to the Crank–Nicolson treatment on the spherical grid.

3. Unladen simulation

The initial condition for the particle–turbulence calculation required a turbulent field that was developed independently on the Cartesian grid. Additionally, the unladen simulation was continued after the developed state was reached, in order to collect statistics for comparison with the laden overset grid calculations. The analytical energy spectrum in (2.3) was used to specify the initial velocity field on the 192^3 Cartesian grid. The non-dimensional input parameters for the simulation were $Re_\lambda = 65$ and $\eta = 0.5$.

The unladen calculation was run for 50 non-dimensional time units with $\Delta t = 0.1$. The development of the turbulence was measured using the velocity derivative skewness

$$Sk = -\frac{\overline{u_{1,1}^3}}{\left(\overline{u_{1,1}^2}\right)^{3/2}} = -\frac{\frac{1}{3}\sum_{i=1}^{3}\overline{(\partial u_i/\partial x_i)^3}}{\left[\frac{1}{3}\sum_{i=1}^{3}\overline{(\partial u_i/\partial x_i)^2}\right]^{3/2}}, \tag{3.1}$$

where the overbar denotes the ensemble average over all cells in the Cartesian grid and the subscripts 1, 2 and 3 identify the vector components in the x, y and z directions, respectively. When Sk reaches its asymptotic value, the flow is considered to be representative of real turbulence. Previous simulations (see Mansour & Wray 1994) have shown that the asymptotic value of Sk in developed turbulence is between -0.4 and -0.5. In this simulation, Sk reached an asymptotic value of -0.48 beginning around $t = 15$. Therefore, the turbulence was assumed to have reached a developed state at $t = 15$.

The isotropy of the unladen turbulence simulation was verified by monitoring the statistics of the velocity field. The time histories of the RMS velocity components were virtually indistinguishable from one another over the length of the simulation, indicating that the turbulence remained isotropic. Another check of isotropy was made by calculating the longitudinal integral scales. These length scales are computed by integrating the two-point spatial correlation of each of the velocity components

$$L_{\alpha\alpha} = \frac{1}{\overline{u_\alpha^2}}\int_0^{L/2}\overline{u_\alpha(\boldsymbol{x})u_\alpha(\boldsymbol{x}+r\boldsymbol{e}_\alpha)}\,\mathrm{d}r \quad \text{for} \quad \alpha = 1, 2, 3, \tag{3.2}$$

where $\boldsymbol{e}_\alpha$ is the unit vector in the α-direction. During the initial development period, ($t \leqslant 15$), the length scales in the three coordinate directions showed different behaviour. However, once the turbulence reached a developed state, the three length scales grew consistently in time from a non-dimensional length of 11 at $t = 15$ to 16

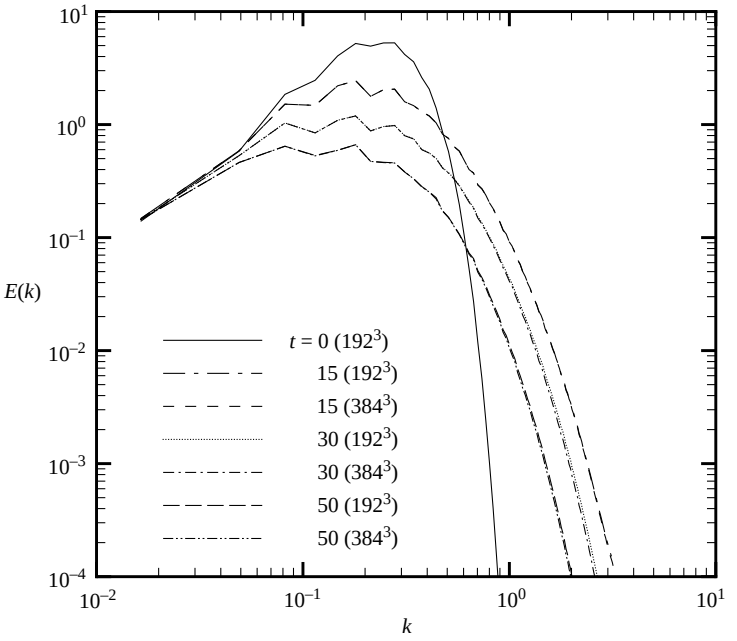

FIGURE 6. Time development of energy spectrum on 192^3 and 384^3 grids.

at $t = 50$. The small deviations in isotropy that were observed can be attributed to the insufficient sample of large-scale motions (see Squires & Eaton 1990*b*).

The Kolmogorov length scale and Taylor microscale, λ, in the unladen simulation initially decayed as the turbulence developed, and then grew as the simulation continued from the developed state. The Taylor microscale Reynolds number initially decayed rapidly as both the Taylor microscale and the RMS velocity components decayed. However, after the turbulence reached a developed state and the Taylor microscale began to grow, the decay of Re_λ was slower.

The temporal development of the spherically symmetric three-dimensional energy spectrum, $E(k)$, is shown in figure 6. The initial analytical spectrum shows that there is very little energy at length scales close to the particle diameter. As the initial condition is advanced toward the developed state at $t = 15$, energy is distributed to higher wavenumbers. After the developed state is reached, the energy spectrum decays in time at all wavenumbers and the peak moves to lower wavenumbers.

The development of the dissipation spectrum, $D(k) = (2/Re)k^2E(k)$, is shown in figure 7. The initial analytical energy spectrum prescribes a peak in the dissipation spectrum near the peak wavenumber of the energy spectrum. In real turbulence, there is separation between the energy-containing scales and the dissipative scales. The initialization period produces this separation of scales as the peaks of the energy and dissipation spectra move in different directions. However, Re_λ is not large enough for an inertial subrange with constant $-5/3$ decay to appear in the energy spectrum. The dissipation spectrum behaves the same way as the energy spectrum after the developed state is reached. The movement of the peak of the dissipation spectrum to lower wavenumbers is consistent with the growth of the Kolmogorov length scale.

The resolution of the large scales in simulations of homogeneous isotropic turbulence can be evaluated from the behaviour of the energy spectrum at low wavenumbers. According to Mansour & Wray (1994), an order of magnitude drop

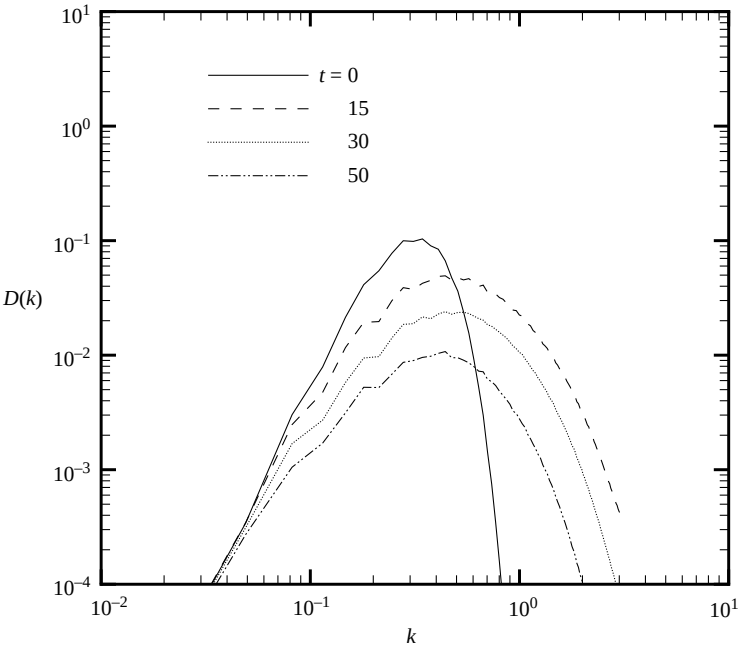

FIGURE 7. Time development of dissipation spectrum.

in the energy spectrum from the value at the peak wavenumber to the value at the lowest resolved wavenumber is ideal in order to guarantee a sufficient sample of energy-containing eddies. The energy spectra in figure 6 at $t = 15$ and $t = 30$ satisfy this criterion. However, the peak of the energy spectrum at $t = 50$ has a value that is only four times the value at the lowest wavenumber. Therefore, the large-scale resolution is marginal at $t = 50$.

The resolution of the small scales is determined by the product of the Kolmogorov length scale and the highest resolved wavenumber, k_{max}. The criterion for adequate resolution of the small scales is $\eta k_{max} \approx 1$. Many homogeneous isotropic turbulence simulations are done with spectral methods, where the highest resolved wavenumber is well defined. For a spectral simulation of the current flow on a 192^3 grid, $\eta k_{max} = 1.57$ at $t = 0$. However, finite-difference techniques do not resolve any non-zero wavenumber exactly, and so it is not clear that the spectral criterion can be applied to a finite-difference simulation. Inadequate resolution of the small scales in a turbulence simulation can lead to energy pile-up at the high wavenumbers (see Mansour & Wray 1994). In order to verify that our small-scale resolution was sufficient, a calculation was done on a 384^3 grid using the developed field from the 192^3 simulation at $t = 15$ as the initial condition. Figure 6 shows good agreement between the energy spectra from the two simulations at the high wavenumbers. Therefore, the flow is adequately resolved at the small scales with the 192^3 grid.

The time histories of turbulent kinetic energy, $q_{ul}^2/2$, and dissipation rate, ε_{ul}, are shown in figure 8. During the unladen simulation, these turbulent statistics were computed from numerical integration of the energy spectrum and the dissipation spectrum. The turbulent dissipation rate initially increases, leading to a decrease in η while the turbulence is developing. The turbulent kinetic energy decays throughout the simulation. Previous simulations of decaying homogeneous isotropic turbulence

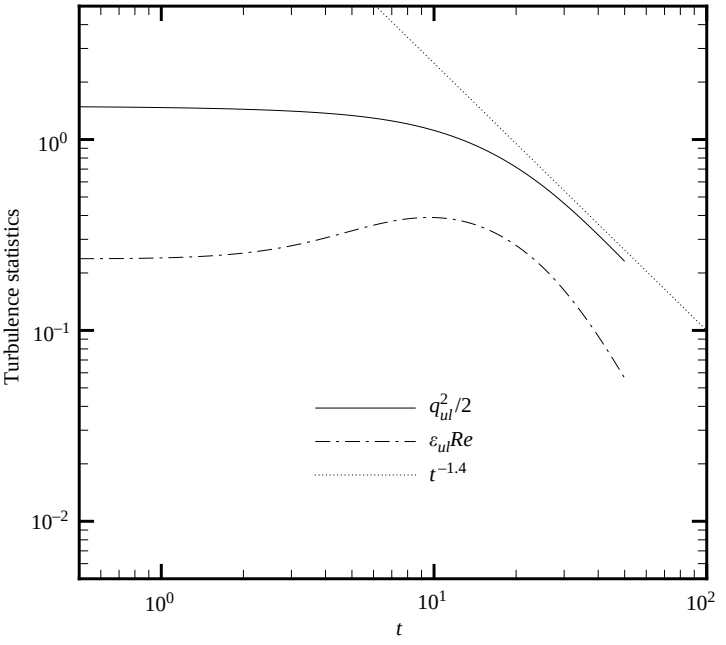

FIGURE 8. Turbulent kinetic energy and dissipation rate time histories.

(see Lee 1985) have shown self-similar decay of the turbulent kinetic energy with a decay exponent in the range $n = 1.33 \sim 1.67$. The dotted line in figure 8 represents a constant decay exponent of 1.4 which was found in the simulation of Squires & Eaton (1990*b*). The unladen simulation in this work did not produce a significant period of self-similar decay of turbulent kinetic energy during the simulation time period. However, the decay exponent is approaching a value consistent with previous work.

For the purposes of comparison with the overset grid simulations where the spectra cannot be computed, the turbulent kinetic energy and dissipation rate from the unladen simulation were also calculated using finite-difference techniques. The turbulent kinetic energy in each cell was calculated using two-point averages of the velocity values at the cell boundary. The turbulent dissipation rate in each cell was calculated by applying two-point averages and second-order-accurate finite differences to the analytical expression for the dissipation rate

$$\varepsilon = \tfrac{1}{2}Re\left[\tau_{xx}^2 + \tau_{yy}^2 + \tau_{zz}^2 + 2\left(\tau_{xy}^2 + \tau_{xz}^2 + \tau_{yz}^2\right)\right], \tag{3.3}$$

where the τ tensor components are the f tensor components without the nonlinear terms. The values calculated in each cell for the turbulent kinetic energy and dissipation rate were averaged to determine finite-difference versions of the time histories in figure 8.

Figure 9 shows time histories of ε_{ul} from the 192^3 and 384^3 calculations of the unladen turbulent flow. The ε_{ul} values are computed using integration of $D(k)$, or the finite-difference technique discussed in the previous paragraph. The spectrally computed ε_{ul} shows sensitivity to the grid resolution, indicating that the small-scale resolution of the unladen simulation is not perfect. The decrease in the spectrally computed ε_{ul} with grid refinement is consistent with the small reduction of the energy

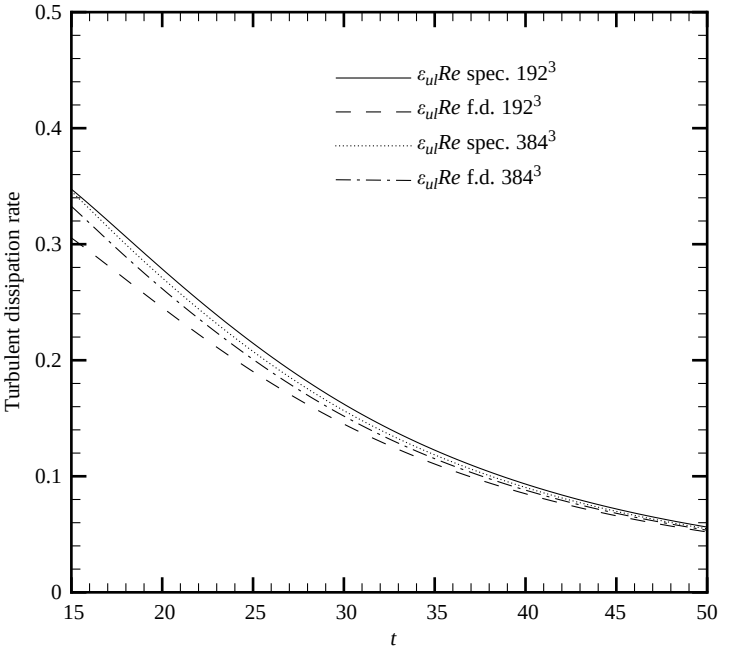

FIGURE 9. Turbulent dissipation rate time histories using different grids and calculation techniques. spec., spectrally computed; f.d., finite difference.

spectrum at high wavenumbers with grid refinement that is shown in figure 6. The computation of ε_{ul} with finite-difference techniques shows an even larger sensitivity to grid resolution owing to the improved numerical approximation of the terms in (3.3) with grid refinement. Similar time histories of $q_{ul}^2/2$ show virtually no sensitivity to the grid resolution or computational technique. The spherical grid provides much higher resolution near the particle than even the 384^3 Cartesian grid. Since the turbulence modification results will focus on the region near the particle, the finite-difference values of $q_{ul}^2/2$ and ε_{ul} from the 384^3 unladen calculation are used to normalize values from the finite-difference computation of the corresponding quantities on the spherical grid in § 4.1.

4. Particle simulations

The behaviour of Sk in the unladen calculation indicated that a developed turbulent state was reached on the Cartesian grid at $t = t_i = 15$. Therefore, this velocity field was used to specify the initial condition for the simulations with the fixed particle using the procedure described in § 2.7. The unladen energy spectrum at $t = 30$ in figure 6 shows good resolution of the large and small scales of the turbulence based on the criteria discussed in § 3. However, at later times, the peak of the energy spectrum is less than an order of magnitude above the value at the lowest wavenumber, indicating inadequate resolution of the large scales. The goal of this work was to perform a fully resolved simulation of particle–turbulence interaction. Therefore, the simulations were run between $t = 15$ and $t = 30$ where the turbulence was developed and adequately resolved at both large and small scales. The properties of the unladen turbulent field at $t - t_i = 0$ and $t - t_i = 15$ are presented in table 5. The particle diameter was approximately twice the unladen Kolmogorov length scale during the simulation.

	$q^2/2$	ε	λ	Re_λ	η
$t - t_i = 0$	0.898	0.042	5.082	32.22	0.455
$t - t_i = 15$	0.572	0.026	5.164	26.12	0.513

TABLE 5. Turbulence statistics from unladen calculation.

The simulations were run on the overset grid described in § 2.2 with $r_{stretch} = 1.02509$. The time step for the simulations was $\Delta t = 0.001$. This time step was set by the stability restriction due to the explicit treatment of the tangential viscous terms in the spherical coordinate momentum equations. Using a smaller time step did not affect the results in any significant way. A measurement of the time scale of the dissipative eddies in the turbulence is given by the Kolmogorov time scale,

$$\tau_k = \sqrt{\frac{\nu}{\varepsilon}}. \tag{4.1}$$

The eddy turnover time from the unladen simulation can be estimated as

$$\tau_e = \frac{\Lambda}{q}, \tag{4.2}$$

where

$$\Lambda = \frac{3\pi}{2q^2} \int_0^\infty \frac{E(k)}{k}\, \mathrm{d}k \tag{4.3}$$

is an estimate of the integral length scale. Using the appropriate values from the unladen simulation at $t = t_i$, the simulation duration, τ_{sim}, is related to the values of these time scales at t_i as

$$\tau_{sim} = 1.78\tau_e(t_i) = 8.82\tau_k(t_i). \tag{4.4}$$

The interaction between the particle and the turbulence depends on the type of turbulent structure into which the particle is placed at the beginning of the simulation. To obtain statistically meaningful measurements of particle–turbulence interaction, we performed a series of simulations with the particle at different points in the turbulent field. The location of the centre of the particle relative to the Cartesian grid was always the same, but the background turbulent field was shifted on its grid so that the particle was located in a different region of the turbulence. The set of simulations included 64 different particle locations chosen from a uniformly spaced $4 \times 4 \times 4$ array. Each of these starting locations is at least $48d_p$ from any other starting location. This distance is more than four times the integral length scale. Therefore, each simulation is assumed to be independent of the others.

In order to verify that the spherical grid provides adequate resolution of the boundary layer at the particle surface, Re_p at each proposed particle location was calculated during the unladen simulation. The maximum value of Re_p over the 64 particle locations at all times was approximately 19. The spherical grid was shown to resolve accurately flows up to at least $Re_\infty = 20$ in § 2.8.1. Therefore, the overset grid system is suitable for these simulations.

4.1. *Turbulence modification results*

During the simulations, the turbulent kinetic energy and dissipation rate were volume-averaged in spherical shells to produce radial profiles. The q^2 and ε profiles from

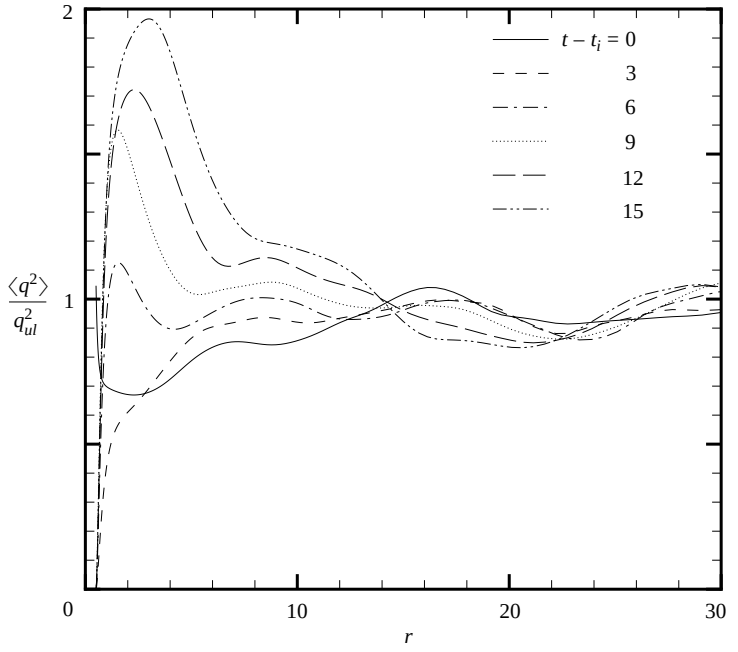

FIGURE 10. Sample volume-averaged turbulent kinetic energy profiles.

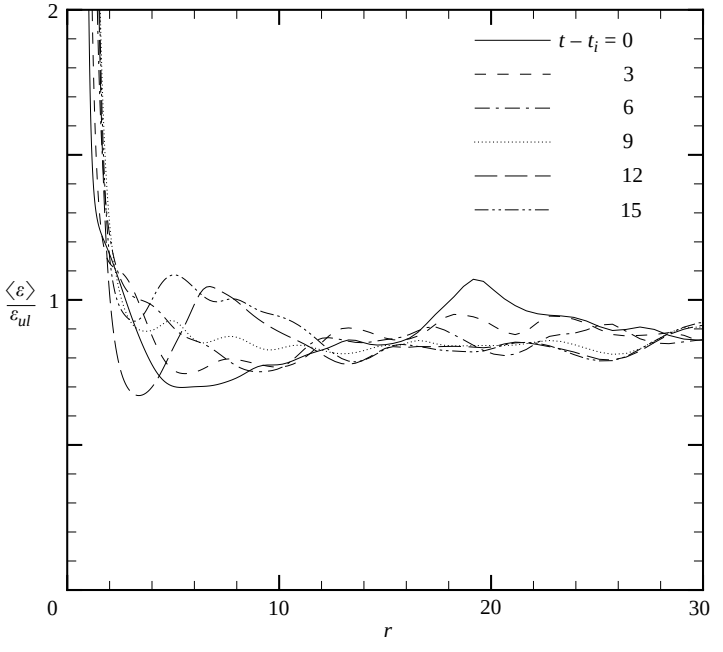

FIGURE 11. Sample volume-averaged turbulent dissipation rate profiles.

one of the simulations, chosen at random from the 64 cases, are shown in figures 10 and 11, respectively. The profiles are each normalized by the values of the unladen turbulent kinetic energy, $q_{ul}^2/2$, and dissipation rate, ε_{ul}, at the same point in time.

There is a sharp rise in the q^2 profile in figure 10 at $t = t_i$ close to the particle surface owing to the projection of the turbulent velocity field interpolated from the Cartesian grid. The projection algorithm forces the radial component of velocity to zero at the particle surface by turning the flow. However, the effect of the no-slip condition is not applied in the tangential and azimuthal directions by the projection. Therefore, the azimuthal and tangential velocity components close to the particle surface increase, producing a higher q^2 near the particle surface. The particle in the sample calculation interacts with a region of high turbulent kinetic energy at later times and dramatically damps q^2 near the particle surface.

Figure 11 shows that ε near the particle surface is substantially higher than the unladen value at all times. The dissipation rate for the spherical coordinate system is defined analytically as

$$\varepsilon = \tfrac{1}{2} Re \left[\tau_{rr}^2 + \tau_{\theta\theta}^2 + \tau_{\phi\phi}^2 + 2 \left(\tau_{r\theta}^2 + \tau_{r\phi}^2 + \tau_{\theta\phi}^2 \right) \right]. \tag{4.5}$$

The enhanced ε near the particle surface can be attributed to the effect of the no-slip boundary condition. In particular, the magnitudes of the radial derivatives of all three velocity components will be higher owing to the presence of the particle. Therefore, τ_{rr}^2, $\tau_{r\theta}^2$ and $\tau_{r\phi}^2$ will be larger. The turning of the flow by the projection algorithm causes the amplified ε at $t = t_i$ by increasing the magnitudes of the azimuthal and tangential velocity components and also the radial derivative of u_r, even though the boundary layer has not yet formed. Therefore, the enhanced dissipation by the particle is due to the displacement of fluid by the particle and the formation of the boundary layer at later times.

The values of q^2 at large radii in figure 10 are similar to the unladen value since the volume integration at large radii samples a large region of the turbulent field. The values of ε at large radii in figure 11 are lower than the unladen value because ε_{ul} was taken from the 384^3 simulation instead of the 192^3 simulation as discussed in § 3. If the smaller value of ε_{ul} from the 192^3 simulation is used for normalization, better agreement between the laden and unladen values of ε at large radii will occur. However, this choice of normalization will cause artificial amplification of the turbulent dissipation rate ratio at small radii which is less desirable as our focus is on the near-particle region.

It is helpful to visualize the behaviour of the turbulence in the laden and unladen cases in order to understand the results shown in the radial profiles. The laden and unladen q^2 contours for the sample case in a plane through the particle centre are shown in figures 12 and 13. The contours are normalized by the value of the unladen turbulent kinetic energy at t_i, $q_{ul}^2(t_i)/2$. The small region of amplified q^2 close to the particle surface owing to the projection of the velocity field at $t = t_i$ can be seen in figure 12. At later times, the particle is surrounded by a region of low turbulent kinetic energy due to the no-slip boundary condition. Structures with high turbulent kinetic energy approach the particle during the simulation, leading to the elevated q^2 inside $r = 10$ shown in figure 10.

The laden and unladen ε contours for the sample case in a plane through the particle centre are shown in figures 14 and 15. The contours are normalized by the value of the unladen turbulent dissipation rate at t_i, $\varepsilon_{ul}(t_i)$. The elevated ε region at $t = t_i$, owing to the projection of the velocity field, is clearly visible in figure 14. The region grows in time, as seen in the profiles in figure 11. At later times, the regions of high ε far from the particle surface have decayed. However, the high ε region close to the particle surface persists throughout the simulation.

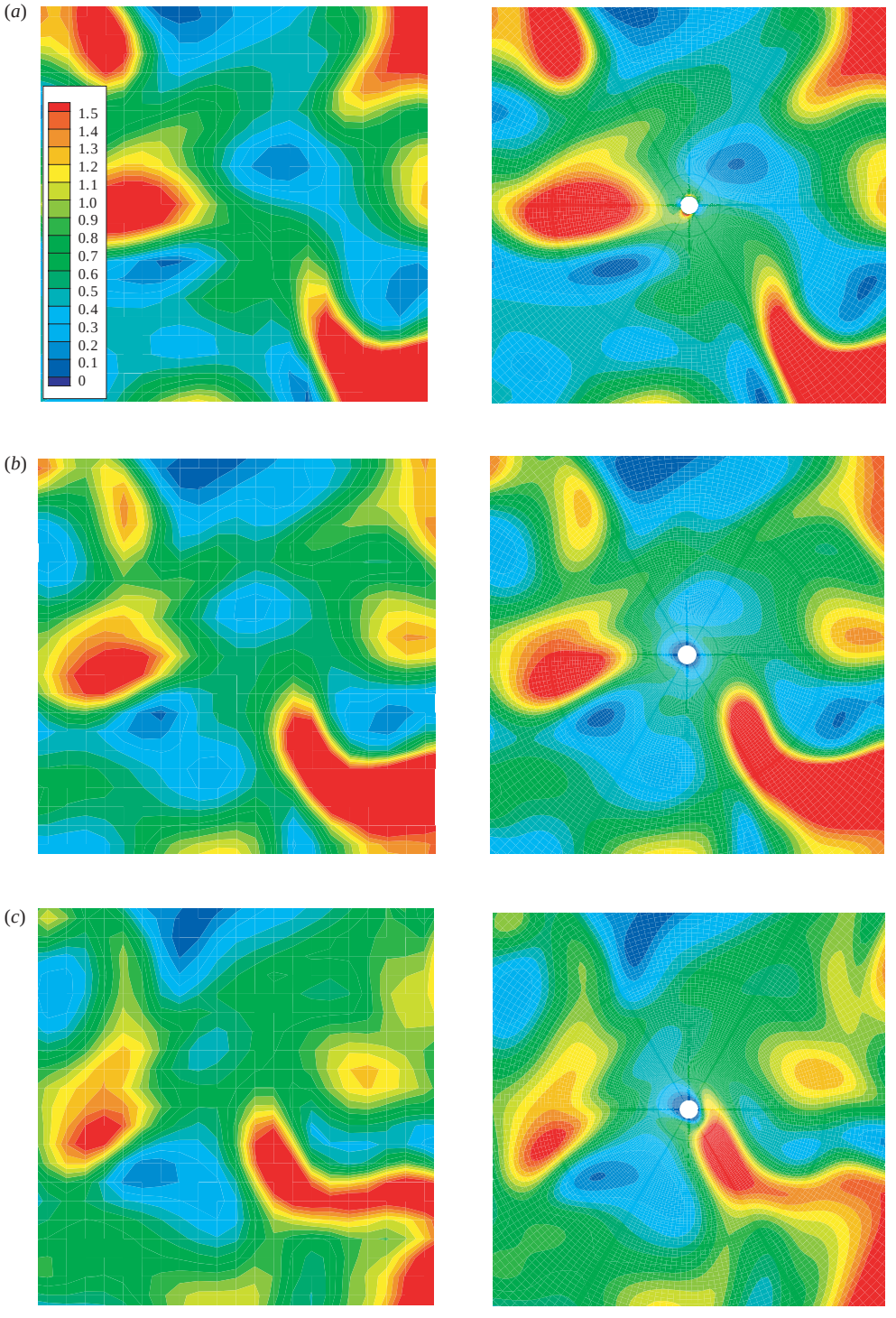

FIGURE 12. Sample turbulent kinetic energy, $q^2/q_{ul}^2(t_i)$, contours in the (x, y)-plane through particle centre at (*a*) $t - t_i = 0$, (*b*) 3 and (*c*) 6.

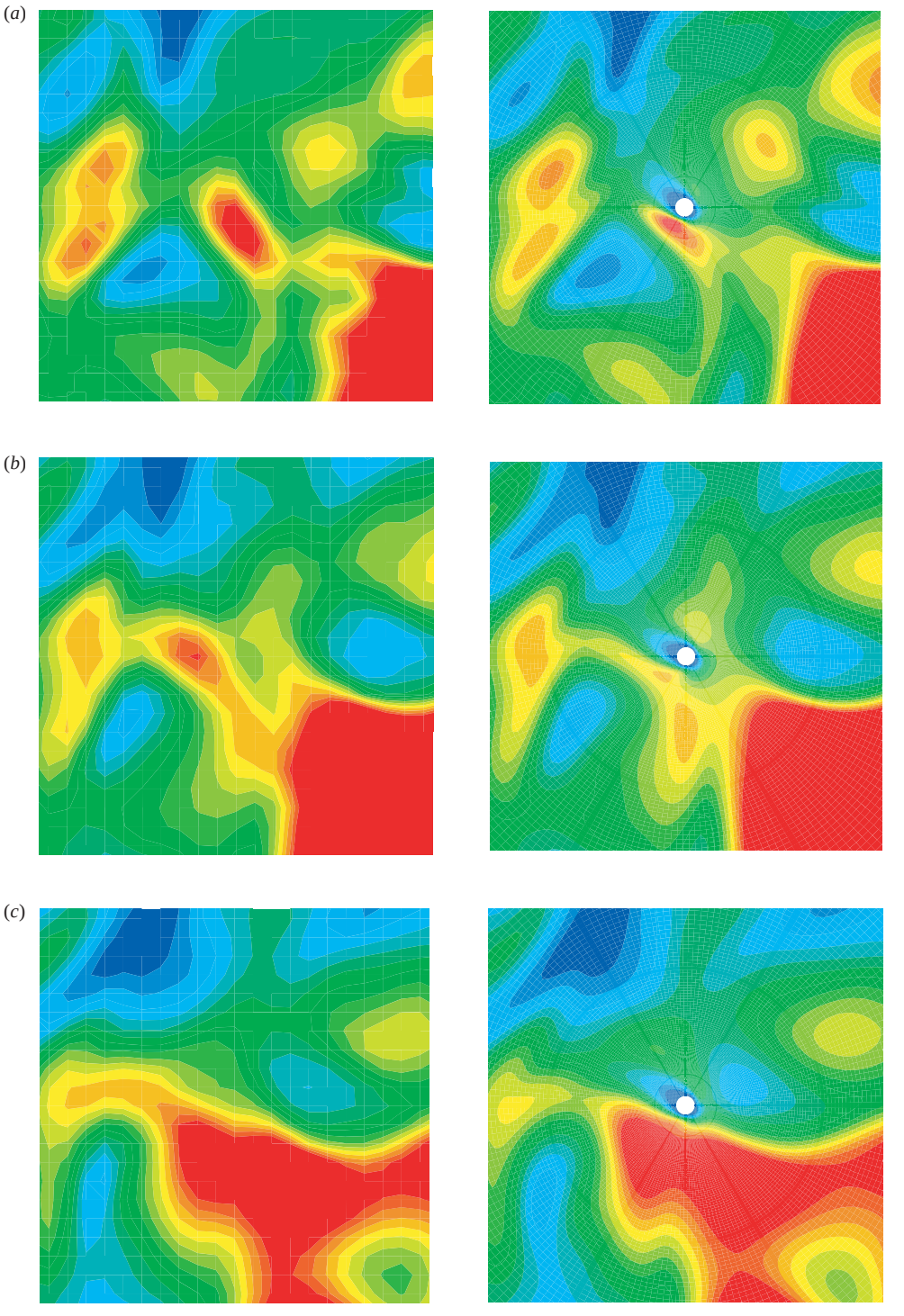

FIGURE 13. Sample turbulent kinetic energy, $q^2/q_{ul}^2(t_i)$, contours in the (x, y)-plane through particle centre at (*a*) $t - t_i = 9$, (*b*) 12 and (*c*) 15.

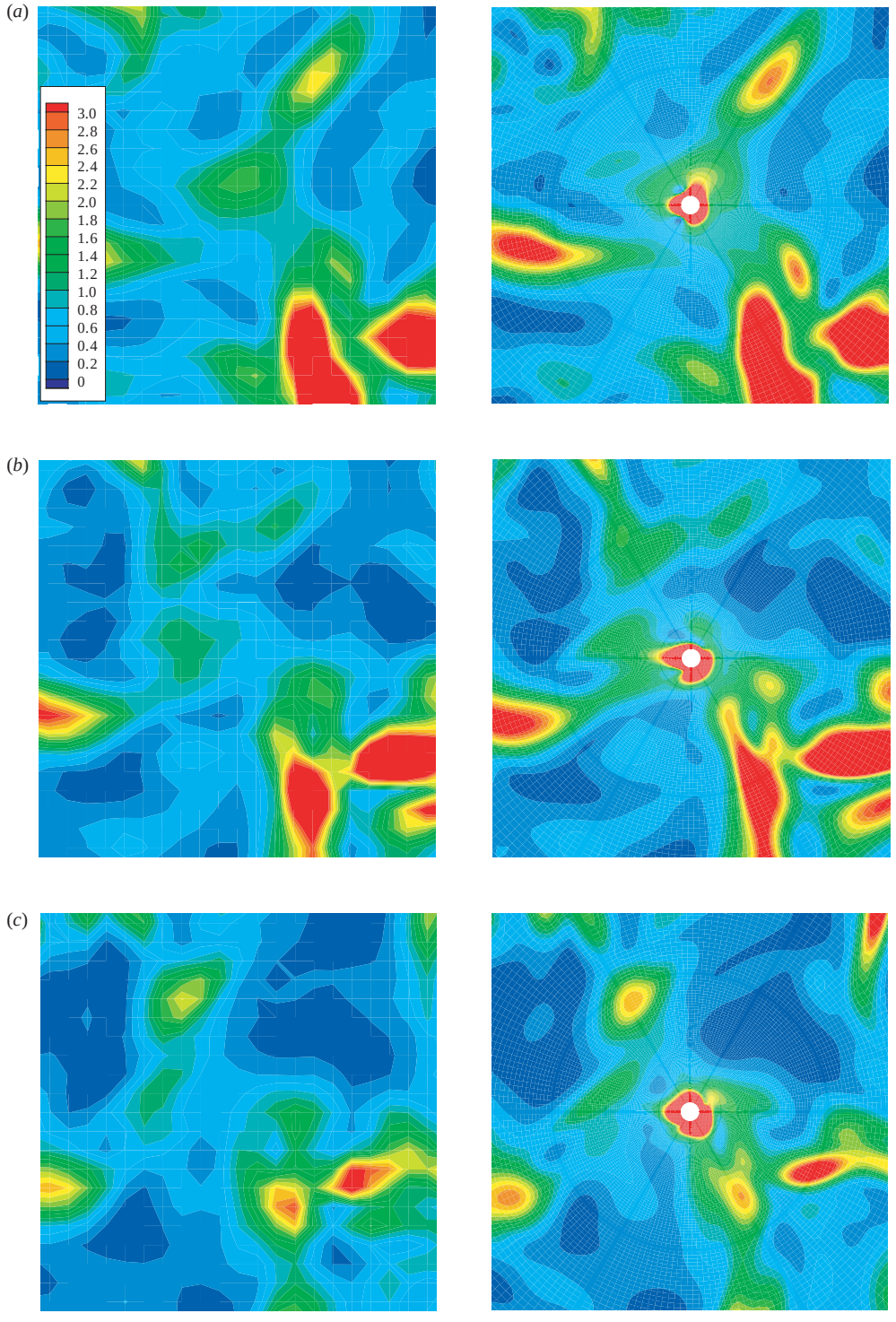

FIGURE 14. Sample turbulent dissipation rate $\varepsilon/\varepsilon_{ul}(t_i)$ contours in the (x, y)-plane through particle centre at (*a*) $t - t_i = 0$, (*b*) 3 and (*c*) 6.

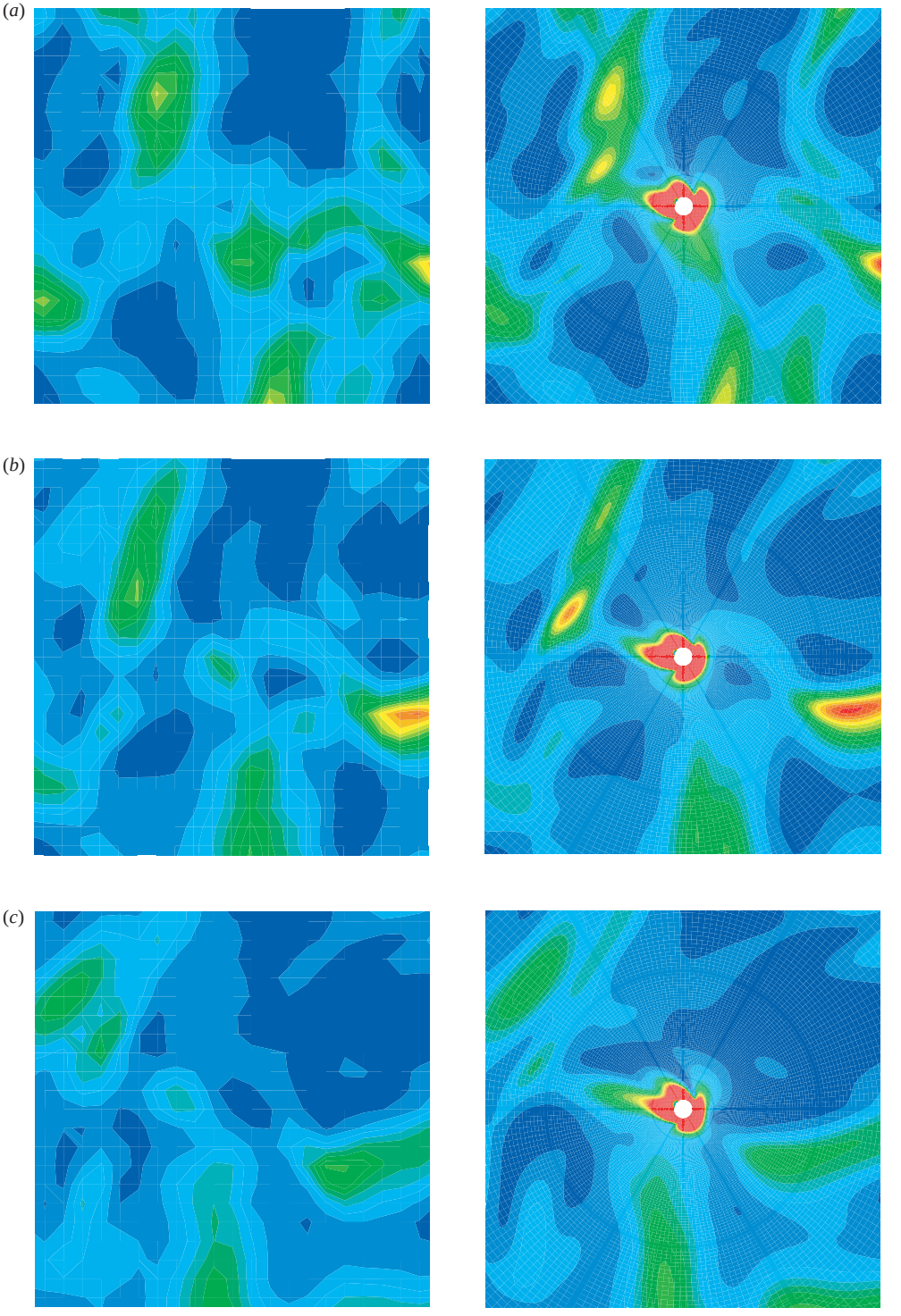

FIGURE 15. Sample turbulent dissipation rate $\varepsilon/\varepsilon_{ul}(t_i)$ contours in the (x, y)-plane through particle centre at (*a*) $t - t_i = 9$, (*b*) 12 and (*c*) 15.

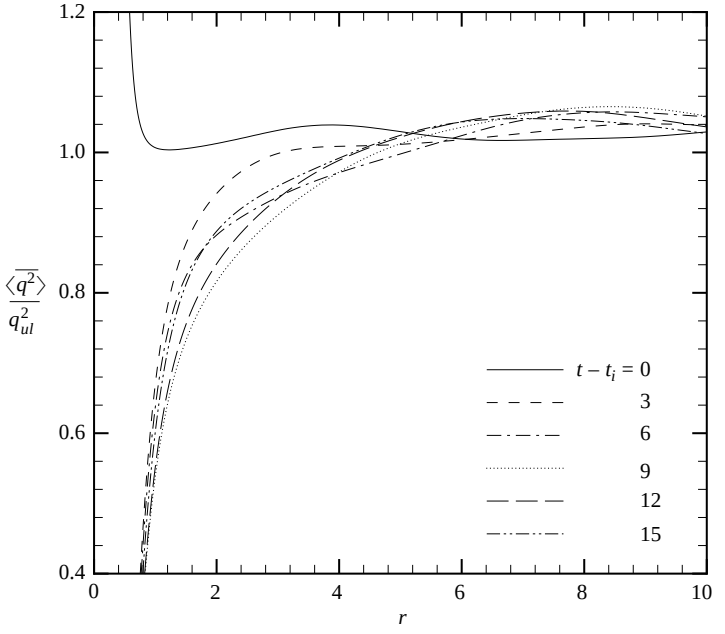

FIGURE 16. Ensemble average of the volume-averaged turbulent kinetic energy profiles.

A comparison of the laden and unladen contours in figures 12–15 shows that the particle has a strong effect on a local region surrounding the particle. This is consistent with the radial profiles in figures 10 and 11. The agreement of the laden and unladen contours away from the particle surface reinforces the previous conclusion that the 192^3 Cartesian grid accurately resolves the turbulent scales in the absence of the particle. The laden calculation resolves the region shown in the contour plots with a much larger number of grid points (see figure 1), but the contours are virtually identical to those from the unladen calculation away from the particle surface.

4.1.1. *Ensemble-averaged results*

The volume-averaged profiles of the turbulent kinetic energy and dissipation rate from each of the 64 simulations were ensemble averaged in an attempt to remove the sensitivity to the local flow structure at small r. The ensemble-averaged q^2 profiles are shown in figure 16. These profiles are within 5 % of the unladen value at most radial locations. Clearly, the ensemble averaging has reduced the fluctuations due to the different turbulent structures with which each particle interacts. Near the surface of the particle, the turbulence has been attenuated significantly. The amplification of q^2 near the particle surface at $t = t_i$ due to the projection of the initial condition is visible in the ensemble average as it was for the sample simulation in figure 10.

The effect of the no-slip boundary condition is felt by the flow as the simulations are advanced in time, creating a region of turbulence attenuation near the particle surface. This region grows as the simulations progress in time, producing a 20 % reduction in the turbulent kinetic energy at $r = 2$ and $t - t_i = 9$. The radial extent of the region of influence of the particle at $t - t_i = 15$ is approximately $r = 4$ although the modification outside $r = 2$ is small. In experiments, particles with $d_p \sim \eta$ have been shown to produce turbulence modification on a much larger scale. The limited effect in these simulations is due to the small volume fraction, $\alpha_p = 7.4 \times 10^{-8}$. Typically,

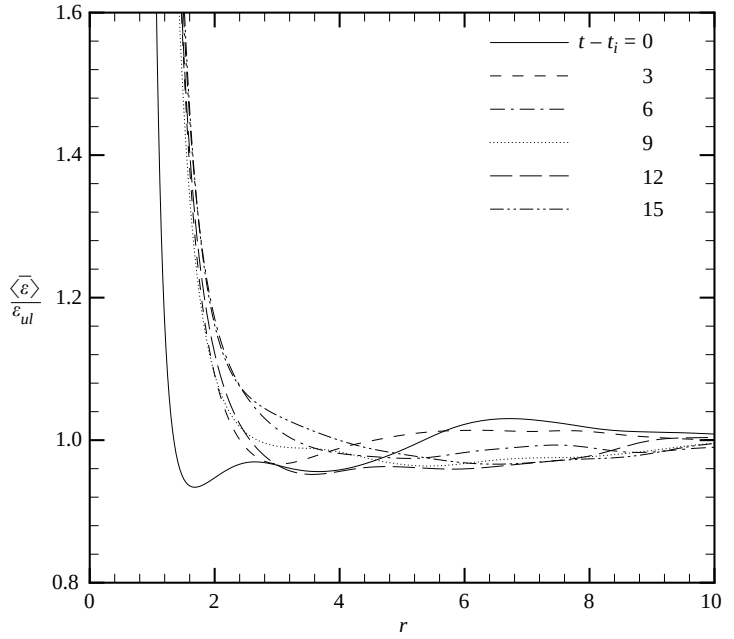

FIGURE 17. Ensemble average of the volume-averaged turbulent dissipation rate profiles.

particle-laden flows which exhibit turbulence modification have an interparticle separation of the order of $10d_p$ whereas the interparticle separation is $192d_p$ in these simulations. Because of the small volume fraction, the particle has a large region from which to draw turbulent kinetic energy before it starts to attenuate the turbulence significantly.

The ensemble-averaged turbulent dissipation rate profiles are shown in figure 17. The amplification of ε near the particle surface at $t = t_i$ due to the displacement of the fluid by the particle is visible in the ensemble average as it was for the sample simulation in figure 11. The region of elevated dissipation adjacent to the particle surface at $t = t_i$ spreads as the simulations are advanced in time. The laden ε value inside $r = 2$ is at least 20 % higher than ε_{ul} at all times after $t = t_i$ in figure 17.

A large ensemble of simulations would produce average turbulent kinetic energy and dissipation rate profiles at $t = t_i$, with only minor fluctuations outside the immediate vicinity of the particle. This is not the case for the average of the dissipation rate profiles from the set of 64 simulations used in this work, as can be seen in figure 17. In order to remove the effect of the deviation in the average initial profile from the desired value of unity, each volume-averaged q^2 and ε profile is first divided by the corresponding volume-averaged profile at t_i. These new profiles are then ensemble averaged and normalized by the ratio of the appropriate unladen value to its value at t_i. These new profiles have the desired value of unity at t_i for all r by definition. The new variables provide a comparison of the decay of the turbulent kinetic energy and dissipation rate in the laden and unladen cases. Whenever the profiles are less than unity, the quantity has decayed faster than in the unladen case and vice versa when the profile values are greater than unity.

The new q^2 profiles are shown in figure 18. The kinetic energy in the laden simulations decayed faster than in the unladen simulation for $r < 5$ until approximately $t - t_i = 9$. However, at $t - t_i = 12$ and $t - t_i = 15$ the profiles

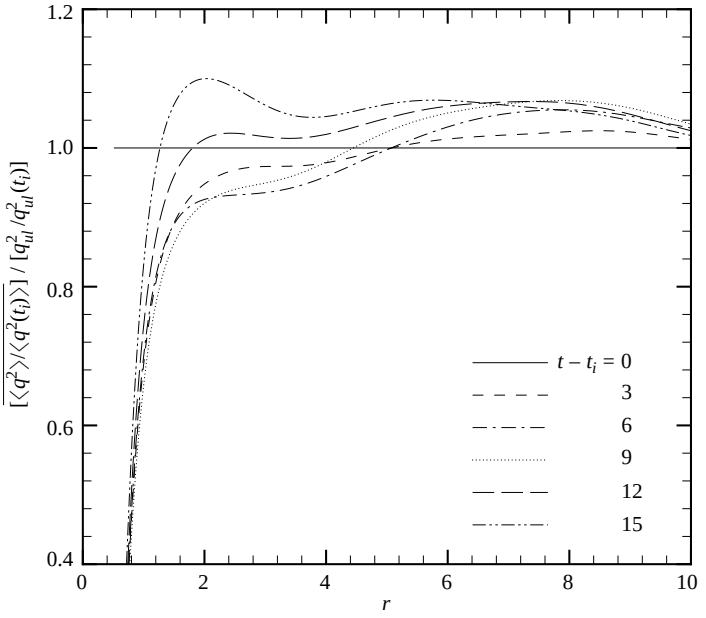

FIGURE 18. Ensemble average of the volume-averaged $t = t_i$-normalized turbulent kinetic energy profiles.

indicate that the average overall decay of q^2 in the laden simulations was slower than the unladen simulation at all radial locations except for the region very close to the particle surface. These results appear to be inconsistent with the profiles in figure 16 which show a reduction of q^2 compared to the unladen simulation at all times for $r < 5$. To investigate the apparent discrepancy, we computed conditional ensemble averages of the volume-averaged q^2 profiles based on the volume-averaged profile at t_i, $\langle q^2(t_i)\rangle$. Cases for which the average value of $\langle q^2(t_i)\rangle$ between $r = 1$ and $r = 5$ was less than $q_{ul}^2(t_i)$ were used to compute ensemble-averaged profiles for a particle starting in a region of low turbulent kinetic energy. Similarly, cases for which the average value of $\langle q^2(t_i)\rangle$ between $r = 1$ and $r = 5$ was larger than $q_{ul}^2(t_i)$ were used to compute ensemble-averaged profiles for a particle starting in a region of high turbulent kinetic energy. The region between the particle surface and $r = 1$ was excluded from the classification criteria owing to the artificial enhancement of the turbulent kinetic energy inside $r = 1$ caused by the initialization. Out of the 64 simulations in this work, 38 satisfied the criterion for the low initial q^2 classification and the remaining 26 were classified as high initial q^2.

The conditional ensemble averages for the low initial q^2 cases are shown in figure 19. At short times, there is an accelerated decay of q^2 compared to the unladen case in the region $r < 4$. However, at later times, the turbulent kinetic energy in the same region shows a reduced decay relative to the unladen case except for the thin region adjacent to the particle surface. This change in behaviour is due to transport of turbulent kinetic energy from the unmodified surrounding fluid. Flow locations where the turbulent kinetic energy initially is low can experience a reduced decay rate of turbulent kinetic energy owing to the transport of energetic turbulent structures from other regions of the flow. The conditional ensemble averages for the high initial q^2 cases are shown in figure 20. The profiles show that there is a consistent accelerated decay of q^2 in the region surrounding the particle. Because the time development

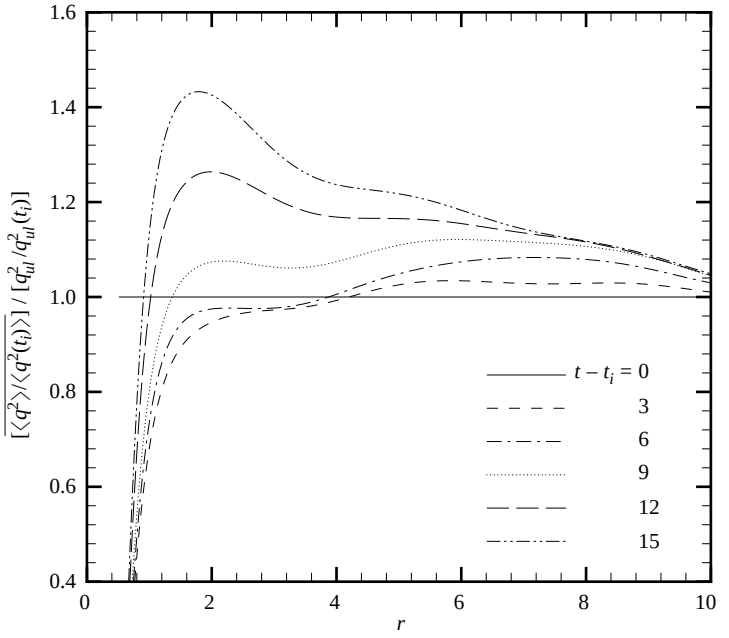

FIGURE 19. Conditional ensemble average of the volume-averaged $t = t_i$-normalized turbulent kinetic energy profiles computed from cases with low initial turbulent kinetic energy.

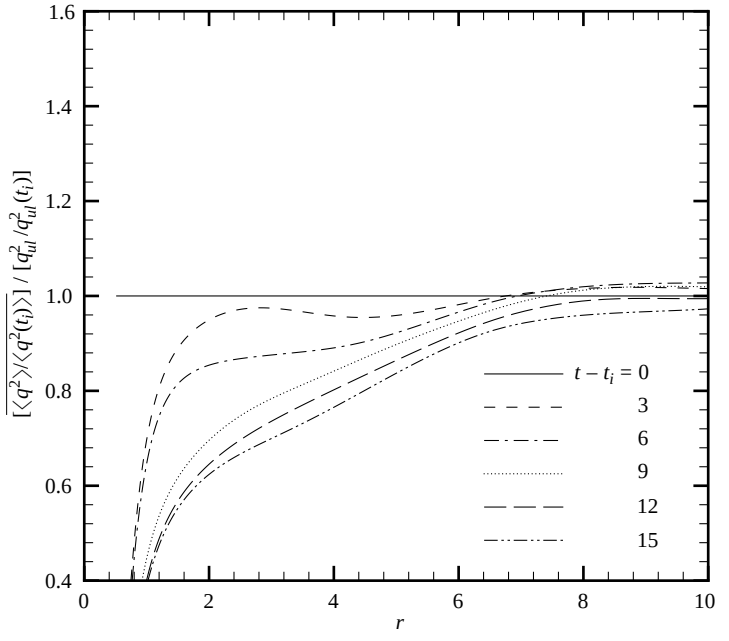

FIGURE 20. Conditional ensemble average of the volume-averaged $t = t_i$-normalized turbulent kinetic energy profiles computed from cases with high initial turbulent kinetic energy.

of the different conditional ensemble averages proceeds in opposite directions, the overall ensemble average shown in figure 18 predicts little change in the average decay rate of q^2 except near the particle surface. As there were more low initial q^2

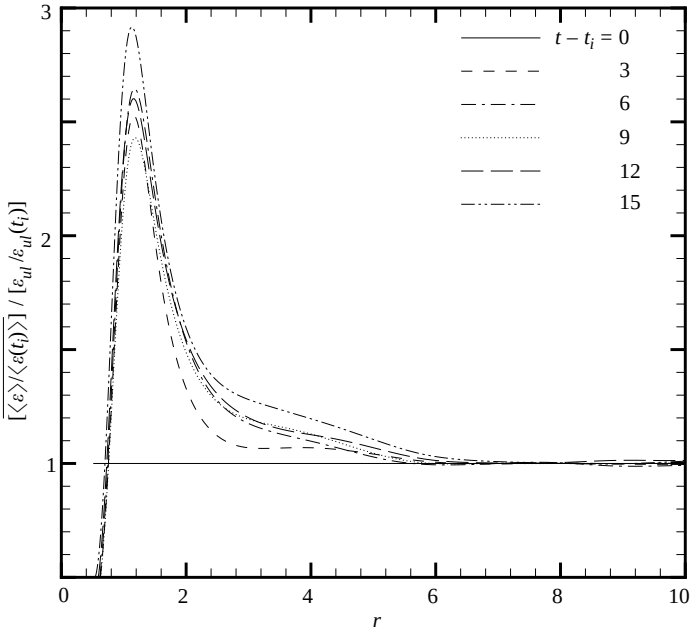

FIGURE 21. Ensemble average of the volume-averaged $t = t_i$-normalized turbulent dissipation rate profiles.

cases, the overall ensemble average is biased towards a reduced decay rate of q^2 at locations away from the particle surface, as shown in figure 18. A larger ensemble of simulations would help to remove the bias and clarify the effect of the particle on q^2 over a larger spatial region.

The difficulty with the data analysis for q^2 is due to the sample size and the small volume fraction in these simulations which causes minimal q^2 modification except for the region very close to the particle surface. The non-monotonic behaviour in time of the profiles in figure 16 and the reduced decay rate outside the near-particle region at later times in figure 18 are due to the competition between turbulence attenuation by the particle and the transport of unmodified turbulence from the surrounding fluid. A larger number of particles would reduce the effect of the transport of unmodified turbulence and would help to elucidate the changes in q^2 outside the near-particle region. A better way to make comparisons of q^2 in the unladen and laden turbulent flows for the single-particle case would be to run unladen overset calculations where the solution on the spherical grid extends to $r = 0$. The radial profiles from the laden calculations could then be normalized by radial profiles from the corresponding unladen overset calculations instead of the box-averaged turbulent statistics from the unladen Cartesian grid simulation. The new proposed normalization will separate the effects of turbulence modification from the volume-averaging and transport effects, and will also help to address the resolution issues associated with the finite-difference computation of ε discussed in § 3.

The ensemble-averaged $t = t_i$-normalized ε profiles are shown in figure 21. The profiles show that in most of the elevated ε region, $r < 2$, the dissipation rate is decaying significantly more slowly than the dissipation rate in the unladen calculation. However, the dissipation rate is decaying faster than the unladen calculation very close to the particle surface. If this behaviour persists at later times, then a larger

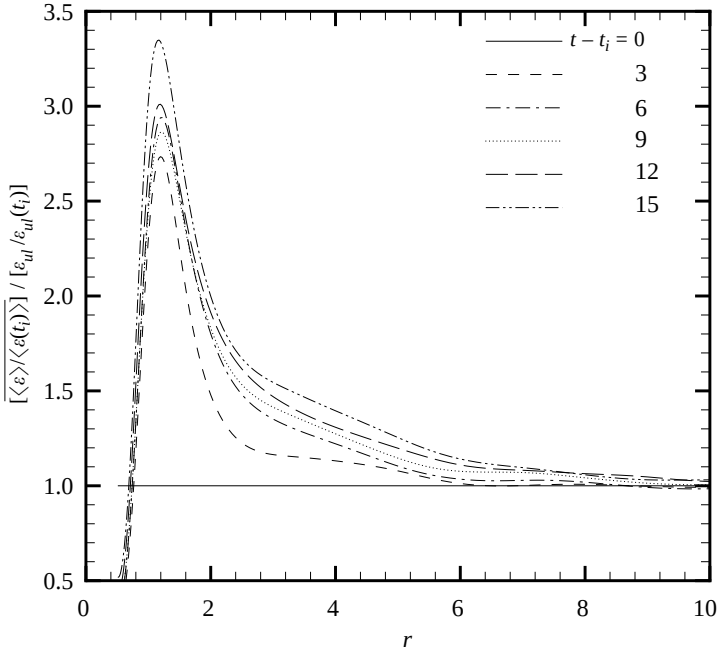

FIGURE 22. Conditional ensemble average of the volume-averaged $t = t_i$-normalized turbulent dissipation rate profiles computed from cases with low initial turbulent dissipation rate.

portion of the increased dissipation due to the presence of the particle will occur away from the particle surface in the local fluid. The width of the region of decelerated turbulent dissipation rate decay is increasing in time, indicating that the particle is modifying a larger region of the turbulence. The persistence of the elevated ε region is visible in the contour plots in figures 14 and 15 where the high ε regions away from the particle surface decay while the high ε region near the particle surface remains visible.

Conditional ensemble averages based on the volume-averaged ε profile at t_i were also computed. Cases for which the average value of $\langle\varepsilon(t_i)\rangle$ between $r = 2$ and $r = 5$ was less than $\varepsilon_{ul}(t_i)$ were used to compute ensemble-averaged profiles for a particle starting in a region of low turbulent dissipation rate. Similarly, cases for which the average value of $\langle\varepsilon(t_i)\rangle$ between $r = 2$ and $r = 5$ was larger than $\varepsilon_{ul}(t_i)$ were used to compute ensemble-averaged profiles for a particle starting in a region of high turbulent dissipation rate. The region between the particle surface and $r = 2$ was excluded from the classification criteria owing to the artificial enhancement of the turbulent dissipation rate inside $r = 2$ caused by the initialization. Out of the 64 simulations in this work, 37 satisfied the criterion for the low initial ε classification and the remaining 27 were classified as high initial ε.

The conditional ensemble averages for the low initial ε cases are shown in figure 22. There is a consistent decelerated decay of ε compared to the unladen case, except for a small region near the particle surface. The conditional ensemble averages for the high initial ε cases are shown in figure 23. The profiles show that there is a decelerated decay of ε inside $r = 2$ (except near the particle surface) and an accelerated decay outside $r = 2$. Because the time development of the different conditional ensemble averages proceeds in the same direction inside $r = 2$, the overall ensemble average

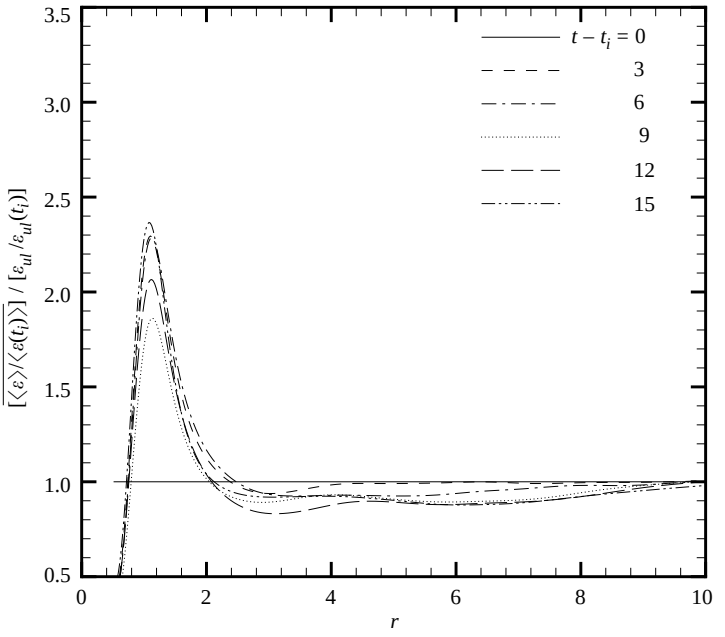

FIGURE 23. Conditional ensemble average of the volume-averaged $t = t_i$-normalized turbulent dissipation rate profiles computed from cases with high initial turbulent dissipation rate.

in figure 21 shows that there is a significant region of slow decay of ε. This region of slow decay is also a region of elevated ε, as shown in figure 17. Therefore, each particle in decaying turbulence will act as a long-lived source of turbulent kinetic energy dissipation.

The ensemble averages of the volume-averaged turbulent kinetic energy and dissipation rate profiles are expected to provide a more accurate representation of the average turbulent behaviour at large r owing to the volume-averaging effect. However, this work is concerned with the behaviour near the surface of the particle where a large amount of turbulence modification occurs. To investigate the quality of the statistical sample, confidence intervals for the ensemble averages were computed. The ensemble averages and the 90 % confidence intervals for the turbulent kinetic energy and dissipation rate at $t - t_i = 9$ are shown in figure 24. The widths of the confidence intervals in the near-particle region, $r < 2$, and far from the particle, $r > 10$, indicate that the statistical sample was sufficient in those regions. However, a larger ensemble of simulations is required in order to reach more definitive conclusions about turbulence modification between $r = 2$ and $r = 10$, as the confidence intervals are significantly wider than the measured modification effect. The width of the confidence intervals shrinks only as one over the square root of the number of samples. Therefore, at least four times the number of samples are required in order to reduce the width of the confidence intervals a significant amount.

4.2. *Particle forces*

The forces applied to the particle by the surrounding turbulent flow were recorded during the overset grid simulations in order to compare with those predicted by a particle equation of motion. Time histories of the three components of the force, non-dimensionalized as shown in (2.6) with U_∞ replaced by u_{rms_0}, from the sample

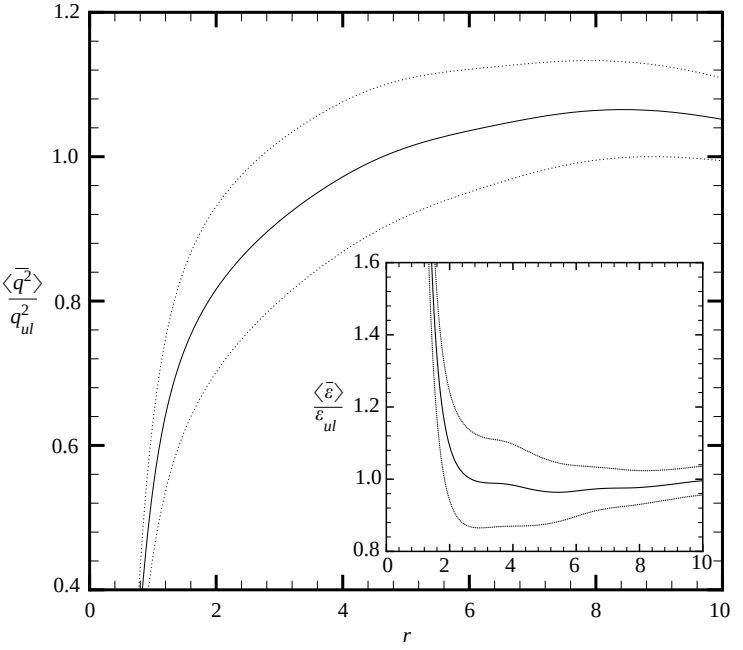

FIGURE 24. Ninety percent confidence intervals for the ensemble average of the volume-averaged turbulent kinetic energy and dissipation rate (inset) profiles at $t - t_i = 9$.

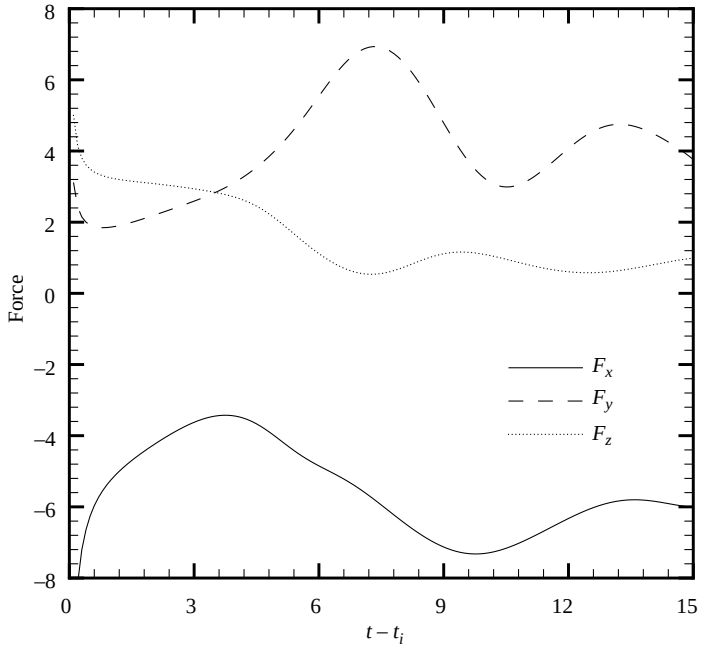

FIGURE 25. Sample force history from overset grid simulation.

simulation are shown in figure 25. The force components at t_i are large owing to the sudden introduction of the particle into the fluid. The force component in the x-direction has the largest magnitude over the course of the simulation. This is

consistent with the flow from right to left shown by the contour plots in figures 12 and 13. The ensemble average of each force component over all 64 simulations was near zero, as expected since the flow direction at the particle location is random. Owing to the isotropic nature of the flow, averaging over all three directions increases the sample size and produces a value closer to the desired value of zero than the average over any single direction.

It is common practice in simulations of turbulent particle-laden flow to use an Eulerian–Lagrangian approach where the motion of the particles is determined by the numerical integration of a particle equation of motion. The particle equation of motion, (1.1), predicts that the non-dimensional forces applied to a fixed particle by the turbulent field are

$$\begin{aligned} \boldsymbol{F}_{total} &= \frac{24}{Re}\boldsymbol{u}\left[1+0.15Re_p^{0.687}\right] + \frac{24}{Re}K_1(t-t_i)\boldsymbol{u}(t_i) \\ &\quad + \frac{24}{Re}\int_0^{t-t_i} K(t-t_i-\tau,\tau)\frac{\mathrm{d}\boldsymbol{u}}{\mathrm{d}\tau}\mathrm{d}\tau + 2\frac{\mathrm{D}\boldsymbol{u}}{\mathrm{D}t} \\ &= \boldsymbol{F}_d + \boldsymbol{F}_{ivd} + \boldsymbol{F}_h + \boldsymbol{F}_{ami}, \end{aligned} \tag{4.6}$$

where $\boldsymbol{F}_d$ is the drag contribution, $\boldsymbol{F}_{ivd}$ is the portion of the history term accounting for the initial velocity difference between the particle and the fluid, $\boldsymbol{F}_h$ is the remainder of the history term, and $\boldsymbol{F}_{ami}$ is the combination of the added mass term and the undisturbed fluid pressure gradient and viscous stress term. There are two different Reynolds numbers in (4.6); Re is the Reynolds number based on the velocity used for non-dimensionalization, u_{rms_0}, while Re_p is based on the magnitude of the slip velocity, $|\boldsymbol{u}|$.

The history kernel of Kim *et al.* (1998) is used to specify $K(t-t_i-\tau,\tau)$ and $K_1(t-t_i)$. The initial velocity difference term is singular at $t = t_i$. Therefore, the force due to this term cannot be numerically evaluated at $t = t_i$. The infinite force corresponds to the formation of a thin layer of vorticity when the particle is suddenly introduced into the flow. However, the initial velocity term is integrable, producing a finite effect on the particle velocity if it is allowed to move. The upper limit of the history integral is also singular. Therefore, the modified numerical integration procedure described by Kim *et al.* (1998) is used to calculate $\boldsymbol{F}_h$.

To evaluate the forces in (4.6), the undisturbed fluid velocity at the particle location must be computed. These velocities and the appropriate time derivatives are obtained from the unladen turbulent simulation. The particle centre for each overset grid calculation was a Cartesian grid pressure node. Therefore, the components of velocity and the computed time derivatives at the neighbouring staggered grid velocity nodes are averaged to give the required values at the particle centre. These values are available at the discrete time intervals provided by the unladen turbulent calculation. The time step for the unladen simulation was chosen so that the turbulence statistics were not changed by any further reduction in its value. However, this does not guarantee that evaluation of the forces in (4.6) will not change as the time step is reduced. To verify that the computed forces were resolved in time, the results from the unladen simulation with $\Delta t = 0.1$ were compared to an unladen simulation with $\Delta t = 0.025$. The finer time step caused small changes in the time histories of $\boldsymbol{F}_{ami}$ and $\boldsymbol{F}_h$, but the other two forces were virtually identical to the results from the $\Delta t = 0.1$ simulation. Since the drag and initial velocity difference forces were much larger than the other forces, the effect of the reduction of the time step on the total force predicted

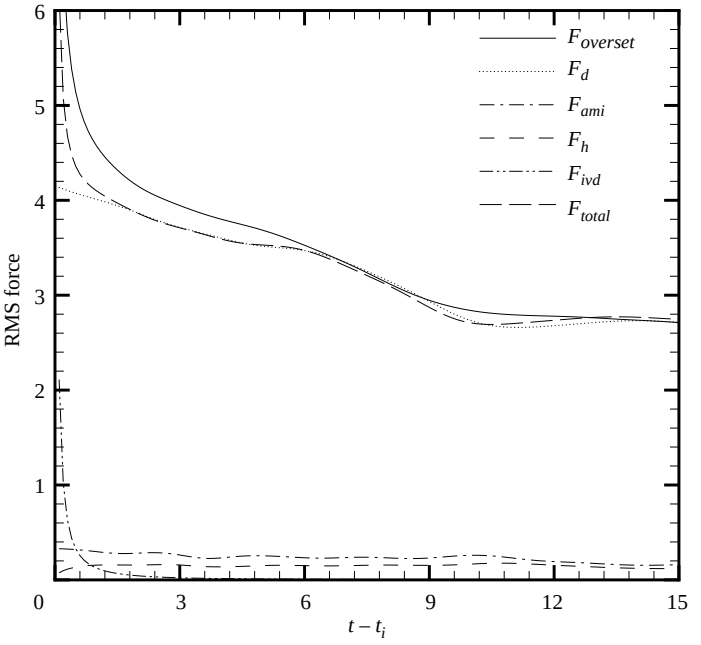

FIGURE 26. RMS force on particle predicted by terms in the particle equation of motion.

by the particle equation of motion was negligible. Therefore, the forces computed from the $\Delta t = 0.1$ simulation were assumed to be accurately resolved in time and were used for comparison with the forces from the overset grid simulations.

The RMS force history from the overset grid simulations and the various components of the RMS force predicted by (4.6) are shown in figure 26, where the RMS values are computed over all three component directions. The effect of the initial condition decays very rapidly and after $t - t_i = 1$, the RMS force decays gradually with the turbulence. The drag force is clearly the dominant term in the particle equation of motion. The initial velocity difference term is significant at short times. However, the history force and the added mass and undisturbed fluid stress force are small fractions of the total force throughout the duration of the simulation. Bagchi & Balachandar (2003*a*) found that the added mass and history forces did not improve predictions of the force on a fixed particle in streaming turbulence with $d_p \sim \eta$ and concluded that the standard drag correlation without the added mass and history forces provided the closest approximation to the DNS result. Kim *et al.* (1998) also found that the drag force was the dominant term for high-density particles injected into a stagnant or oscillating flow. The total RMS force predicted by the particle equation of motion in figure 26 is less than that calculated from the results of the overset grid simulations at most times. The total RMS force is also approximated well by the RMS drag force after the initial velocity difference term decays. In many simulations that use a particle equation of motion to track point particles, the particles are introduced into the fluid domain with the same velocity as the fluid. In those cases, the initial velocity difference term can be ignored.

Time histories of the RMS errors between the force on the particle from the overset grid simulations and the force predicted by the drag term from the particle equation of motion are shown in figure 27. Each of the time histories is normalized by the RMS force over all three component directions from the overset grid simulation set.

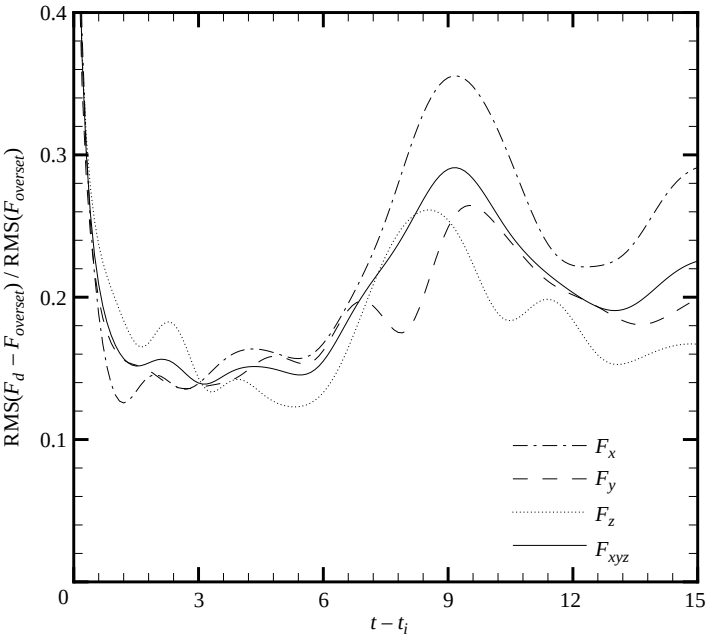

FIGURE 27. RMS force error considering only the drag term in the particle equation of motion.

The RMS errors for each of the components of force are all similar to each other and therefore similar to the RMS error computed over all three components. Initially, a large error is present because the force due to the initial velocity difference is not included. When the initial velocity difference force is included, the error at short times is reduced substantially, as shown in figure 28. The RMS error at later times and some of the fluctuations in the error time histories are reduced by inclusion of the added mass and undisturbed fluid stress forces, as shown in figure 29. Finally, the time histories of the RMS error in the force between the overset grid simulation and all terms of the particle equation of motion are shown in figure 30. There is no significant improvement by the inclusion of the history integral term.

Based on the RMS error time histories in figures 27–30, the best estimate of the force applied to a particle in a turbulent field comes from the combination of $\boldsymbol{F}_d$, $\boldsymbol{F}_{ivd}$ and $\boldsymbol{F}_{ami}$ from (4.6). The RMS errors using this combination are between 15 % and 30 % of the correct RMS force on the ensemble of particle locations. By inserting a particle into the flow domain with the same velocity as the local fluid, $\boldsymbol{F}_{ivd}$ can be ignored. The history integral term is cumbersome to compute as part of a point-particle tracking algorithm and the results of this work and those of Bagchi & Balachandar (2003*a*) indicate that it does not improve the prediction of the force on the particle. This result is not surprising as the form of the history kernel used in this work was developed and optimized in a uniform flow (see Kim *et al.* 1998). When the particle diameter is the same order as the Kolmogorov length scale, the flow over the particle cannot be considered to be uniform.

The deficiency of (4.6) in predicting the correct RMS force on the particle is due to the particle size considered in this work. Much of the derivation of the particle equation of motion is based on the assumption that the particle is significantly smaller than any of the flow scales of interest. However, many particle-laden flows contain

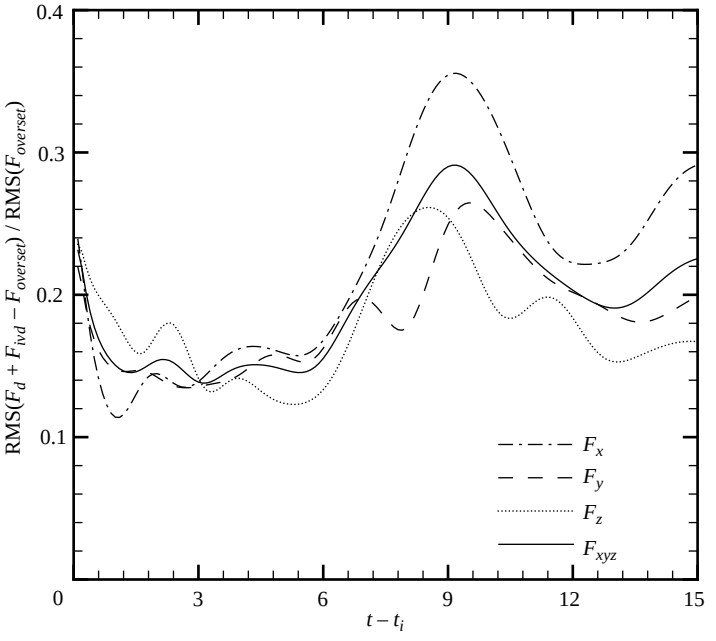

FIGURE 28. RMS force considering the drag and initial velocity difference terms in the particle equation of motion.

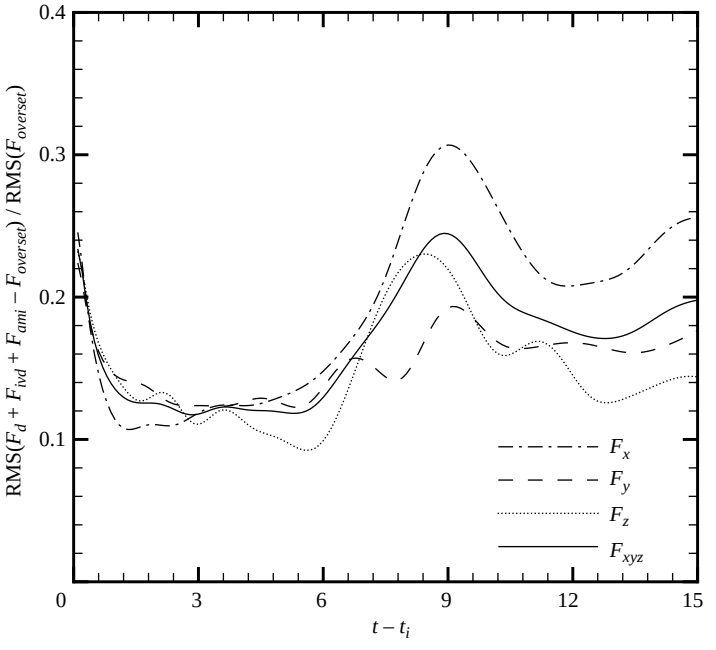

FIGURE 29. RMS force error considering all terms in the particle equation of motion except the history integral.

particles with diameters of the same order as the Kolmogorov length scale. Therefore, some modification to the particle equation of motion is expected in order to simulate accurately these physically relevant flows. When the particle diameter is of the same

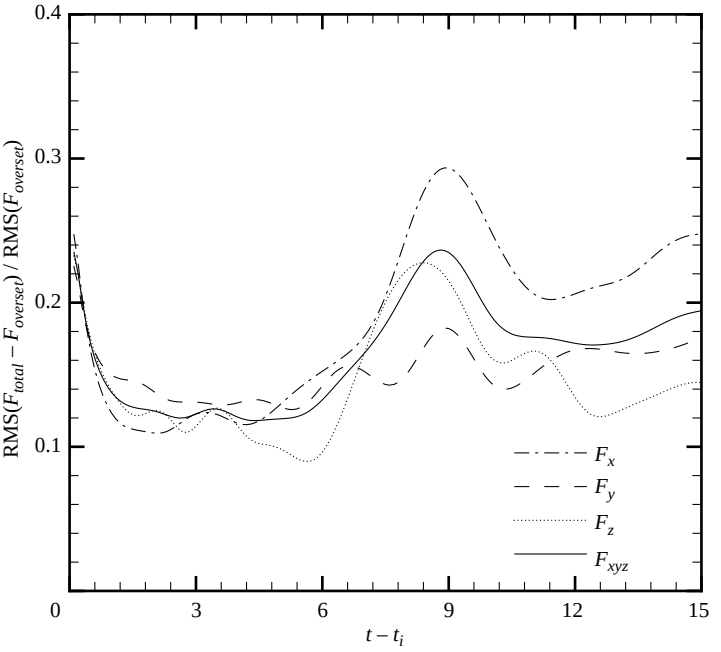

FIGURE 30. RMS force error considering all terms in the particle equation of motion.

order as the Kolmogorov length scale, the variation in the flow across the particle can be significant. Therefore, a drag correlation determined from uniform flow simulations and experiments will not accurately predict the drag force in this case or any other where a distorted wake develops as a result of flow variations on the scale of the particle diameter.

The drag term was shown to be the dominant term in the particle equation of motion in this work and other studies of the forces on a relatively dense particle (see Kim *et al.* 1998; Bagchi & Balachandar 2003*a*). Therefore, efforts to improve predictions by the particle equation of motion should be focused on the development of a modified drag term. Any useful correction to the drag term will most likely be stochastic in nature. The deterministic modification to the drag term derived by Bagchi & Balachandar (2003*b*) for axisymmetric and planar straining flows is a complex expression that is only useful for a relatively simple class of flows. It is doubtful that a similar expression could be determined for fully turbulent flows. Additionally, many simulations of turbulent particle-laden flow are done with large-eddy simulation (LES) where the resolved strain rate and other properties of the velocity field at the particle location are not readily available. In this type of unresolved simulation, the application of a deterministic model would require stochastic approximation of subgrid-scale velocity information. Therefore, a stochastic model for the drag modification would be more useful for DNS and LES simulations with point-particle tracking. The development of a suitable stochastic model will require fully resolved simulations over a range of particle diameters and Taylor microscale Reynolds numbers.

5. Conclusions

An overset grid technique was used to simulate the interaction between a fixed particle and decaying homogeneous isotropic turbulence with resolution of all scales

of fluid motion. An ensemble of 64 simulations with the particle inserted into a different region of the same developed turbulent field was used to determine statistics for turbulence modification and the forces on the particle. The particle diameter was approximately twice the Kolmogorov length scale of the unmodified turbulence and the particle Reynolds numbers due to the turbulent fluctuations had a maximum value close to 20. The simulation duration for each realization was almost two eddy turnover times.

During each simulation, radial profiles of the turbulent kinetic energy and dissipation rate were obtained by volume averaging over spherical shells. Ensemble averages of the turbulent kinetic energy profiles reveal significant attenuation within one diameter of the particle surface. The ensemble averages of the turbulent dissipation rate profiles show an enhanced dissipation rate region with a significantly decelerated dissipation decay rate within 1.5 diameters of the particle surface. The ensemble averages showed minor turbulence modification outside 5 diameters from the particle surface owing to the small volume fraction. These results indicate that the displacement of fluid by the presence of the particle and the formation of the boundary layer at the particle surface lead to turbulence modification in a local region. In order to reproduce the global turbulence modification seen in experiments, a number of particles of $O(1000)$ are probably required.

The forces applied to the particle during the simulations were recorded and compared to those predicted by a Lagrangian particle equation of motion. The drag force in the particle equation of motion was shown to be the dominant term. The initial velocity difference force was significant at short times, while the added mass and undisturbed fluid stress term and the history integral term were both small fractions of the total force. RMS errors between the forces from the overset grid simulation and the forces predicted by combinations of terms in the particle equation of motion were computed. The combination of the drag term, added mass and undisturbed fluid stress term, and the initial velocity difference term produced RMS errors that were between 15 % and 30 % of the RMS force from the fully resolved simulation set. The inclusion of the history term did not produce any improvement in the force prediction by the particle equation of motion. The discrepancy between the force predicted by the particle equation of motion and the force from the overset grid simulations is due to the size of the particle relative to the Kolmogorov length scale. The derivation of the particle equation of motion assumes that the particle diameter is smaller than any flow scales of interest. Therefore, the assumptions of flow uniformity in the neighbourhood of the particle are invalid for the particles in this work.

The drag force was the dominant term in the particle equation of motion. Therefore, this term should be the focus of efforts to improve the prediction of the forces on a particle in a turbulent flow by the particle equation of motion. It would be extremely difficult to develop a deterministic model for the modification to the standard drag force based on the turbulent flow variation across the particle. Therefore, a stochastic model for the correction to the standard drag force should be developed. This model would be dependent on the ratio of the particle diameter to the Kolmogorov length scale and its effect would vanish as the particle diameter became significantly smaller than the Kolmogorov length scale. Multiple sets of simulations, similar to those performed in this work, over a range of Taylor microscale Reynolds numbers and particle diameters are required in order to develop a suitable stochastic model. This work has shown that the particle equation of motion underpredicts the RMS force on the particle. It is unlikely that a stochastic model could significantly reduce the

RMS error in the prediction of the force by the particle equation of motion. However, the model could raise the RMS force predicted by the particle equation of motion, thereby improving estimates of particle dispersion in simulations with point-particle tracking.

This work was supported by the Department of Energy ASCI ASAP program under contract B523583 from the Lawrence Livermore Laboratory. Opinions expressed in this report are those of the authors and not those of Stanford University, the Lawrence Livermore Laboratory, or the Department of Energy. This work was supported in part by a grant of computer time from the DOD High Performance Computing Modernization Program at the Naval Research Laboratory-DC.

Appendix. Spherical coordinate spatial discretization

A.1. *Pole Treatment*

The poles of the spherical coordinate system ($\theta = 0, \pi$) require careful treatment to guarantee a well-behaved numerical solution to the governing equations. The staggered grid system places only u_θ nodes on the poles. Since the terms in the spatially discretized u_θ equation cannot be evaluated numerically owing to the coordinate singularity, a different approach is required to determine u_θ at the poles. The relationship between Cartesian and spherical velocity components provides the following equations for u_θ and u_ϕ at the poles:

$$u_\theta(\phi; r; \theta = 0, \pi) = (w \sin\phi + v \cos\phi)\cos\theta, \tag{A 1a}$$

$$u_\phi(\phi; r; \theta = 0, \pi) = w \cos\phi - v \sin\phi. \tag{A 1b}$$

Since the Cartesian velocity components are independent of ϕ at the poles, (A 1*a*)–(A 1*b*) can be Fourier transformed in the ϕ-direction to determine the Fourier coefficients for the non-zero mode ($k_\phi = 1$) at the poles. The Fourier coefficients for u_θ and u_ϕ are related at the poles,

$$\hat{u}_\theta\left(k_\phi = 1; r; \theta = 0, \pi\right) = -\mathrm{i}\hat{u}_\phi\left(k_\phi = 1; r; \theta = 0, \pi\right)\cos\theta, \tag{A 2}$$

where $\mathrm{i} = \sqrt{-1}$. Therefore, u_θ at the poles is determined by interpolating u_ϕ to the poles with a two-point average, computing the Fourier transform, and then using (A 2).

The components of the f tensor must be finite in the entire spherical solution domain since the viscous stresses and the velocity components are finite. Therefore, the singular terms that make up some of the f tensor components analytically combine or cancel to ensure that the f tensor components are finite at the poles. With a numerical treatment, the analytical cancellation of singular terms cannot occur, and the calculation of the f tensor components at the poles must be handled differently from the calculation in the rest of the spherical domain. Fortunately, only the $f_{\theta\phi}$ component,

$$f_{\theta\phi} = \frac{1}{Re}\left[\frac{1}{r}\frac{\partial u_\phi}{\partial\theta} - \frac{u_\phi \cot\theta}{r} + \frac{1}{r\sin\theta}\frac{\partial u_\theta}{\partial\phi}\right] - u_\theta u_\phi, \tag{A 3}$$

must be computed at the poles. Taking the limit of (A 3) and using (A 1*a*)–(A 1*b*) and L'Hospital's rule, the non-singular expression for $f_{\theta\phi}$ at the poles is

$$\lim_{\theta\to 0,\pi} f_{\theta\phi} = \frac{1}{Re}\left[\frac{1}{r\cos\theta}\frac{\partial^2 u_\theta}{\partial\theta\partial\phi}\right] - u_\theta u_\phi. \tag{A 4}$$

The discretized version of (A 4) is obtained using second-order-accurate central differences and two-point averages. All differencing and averaging across the poles is done using the procedure described by Mohseni & Colonius (2000).

A.2. *Particle surface treatment*

The radial derivatives in the spherical coordinate f tensor components cannot be computed with central differences at the particle surface. One-sided second-order-accurate finite-difference techniques are used instead to calculate the radial derivatives in $f_{r\theta_{i,0,k}}$ and $f_{r\phi_{i,0,k}}$. The one-sided difference stencil must be chosen so that the truncation errors will combine properly with the truncation errors from the central difference calculations of $f_{r\theta_{i,1,k}}$ and $f_{r\phi_{i,1,k}}$, in order to guarantee second-order accuracy in the evaluation of terms which are radial derivatives of $f_{r\theta}$ and $f_{r\phi}$. The one-sided difference stencil for the $(\partial/\partial r)(u_\theta/r)$ term in $f_{r\theta}$ uses values of u_θ/r at the particle surface and the next three radial locations. The same treatment is used for the evaluation of $(\partial/\partial r)\left(u_\phi/r\right)$ in the calculation of $f_{r\phi}$ at the particle surface.

REFERENCES

Bagchi, P. & Balachandar, S. 2002*a* Effect of free rotation on the motion of a solid sphere in linear shear flow at moderate *Re*. *Phys. Fluids* **14**, 2719–2737.

Bagchi, P. & Balachandar, S. 2002*b* Shear versus vortex-induced lift on a rigid sphere at moderate *Re*. *J. Fluid Mech.* **473**, 379–388.

Bagchi, P. & Balachandar, S. 2002*c* Steady planar straining flow past a rigid sphere at moderate Reynolds number. *J. Fluid Mech.* **466**, 365–407.

Bagchi, P. & Balachandar, S. 2003*a* Effect of turbulence on the drag and lift of a particle. *Phys. Fluids* **15**, 3496–3513.

Bagchi, P. & Balachandar, S. 2003*b* Inertial and viscous forces on a rigid sphere in straining flows at moderate Reynolds numbers. *J. Fluid Mech.* **481**, 105–148.

Bagchi, P. & Balachandar, S. 2004 Response of the wake of an isolated particle to an isotropic turbulent flow. *J. Fluid Mech.* **518**, 95–123.

Boivin, M., Simonin, O. & Squires, K. D. 1998 Direct numerical simulation of turbulence modulation by particles in isotropic turbulence. *J. Fluid Mech.* **375**, 235–263.

Briggs, W. L., Henson, V. E. & McCormick, S. F. 2000 *A Multigrid Tutorial*, 2nd edn. SIAM, Philadelphia, PA.

Burton, T. M. & Eaton, J. K. 2002*a* Analysis of a fractional-step method on overset grids. *J. Comput. Phys.* **177**, 336–364.

Burton, T. M. & Eaton, J. K. 2002*b* High-resolution simulations of particle–eddy interactions. *Powder Technol.* **125**, 104–110.

Burton, T. M. & Eaton, J. K. 2003 Fully resolved simulations of particle-turbulence interaction. *Tech. Rep.* TSD-151. Mechanical Engineering Department, Stanford University.

Chang, E. J. & Maxey, M. R. 1994 Unsteady flow about a sphere at low to moderate Reynolds number. Part 1. Oscillatory motion. *J. Fluid Mech.* **277**, 347–379.

Chang, E. J. & Maxey, M. R. 1995 Unsteady flow about a sphere at low to moderate Reynolds number. Part 2. Accelerated motion. *J. Fluid Mech.* **303**, 133–153.

Chen, S. & Doolen, G. D. 1998 Lattice Boltzmann method for fluid flows. *Annu. Rev. Fluid Mech.* **30**, 329–364.

Clift, R., Grace, J. R. & Weber, M. E. 1978 *Bubbles, Drops, and Particles*. Academic.

Dennis, S. C. R. & Walker, J. D. A. 1971 Calculation of the steady flow past a sphere at low and moderate Reynolds numbers. *J. Fluid Mech.* **48**, 771–789.

Druzhinin, O. A. 2001 The influence of particle inertia on the two-way coupling and modification of isotropic turbulence by microparticles. *Phys. Fluids* **13**, 3738–3755.

Elghobashi, S. 1994 On predicting particle-laden turbulent flows. *Appl. Sci. Res.* **52**, 309–329.

Elghobashi, S. & Truesdell, G. C. 1993 On the two-way interaction between homogeneous turbulence and dispersed solid particles I: Turbulence modification. *Phys. Fluids* A **5**, 1790–1801.

Feng, Z. G. & Michaelides, E. E. 2004 The immersed boundary-lattice Boltzmann method for solving fluid-particles interaction problems. *J. Comput. Phys.* **195**, 602–628.

Ferziger, J. H. & Perić, M. 1996 *Computational Methods for Fluid Dynamics*. Springer.

Fessler, J. R. & Eaton, J. K. 1999 Turbulence modification by particles in a backward-facing step flow. *J. Fluid Mech.* **394**, 97–117.

Ghidersa, B. & Dušek, J. 2000 Breaking of axisymmetry and onset of unsteadiness in the wake of a sphere. *J. Fluid Mech.* **423**, 33–69.

Glowinski, R., Pan, T. W., Hesla, T. I., Joseph, D. D. & Périaux, J. 2001 A fictitious domain approach to the direct numerical simulation of incompressible viscous flow past moving rigid bodies: application to particulate flow. *J. Comput. Phys.* **169**, 363–426.

Gore, R. A. & Crowe, C. T. 1989 Effect of particle size on modulating turbulent intensity. *Intl J. Multiphase Flow* **15**, 279–285.

Harlow, F. H. & Welch, J. E. 1965 Numerical calculation of time-dependent viscous incompressible flow with a free surface. *Phys. Fluids* **8**, 2182–2189.

Hetsroni, G. 1989 Particles–turbulence interaction. *Intl J. Multiphase Flow* **15**, 735–746.

Hu, H. H., Patankar, N. A. & Zhu, M. Y. 2001 Direct numerical simulation of fluid–solid systems using the arbitrary Lagrangian–Eulerian technique. *J. Comput. Phys.* **169**, 427–462.

Johnson, A. A. & Tezduyar, T. E. 1999 Advanced mesh generation and update methods for 3D flow simulations. *Comput. Mech.* **23**, 130–143.

Kim, I., Elghobashi, S. & Sirignano, W. A. 1993 Three-dimensional flow over two spheres placed side by side. *J. Fluid Mech.* **246**, 465–488.

Kim, I., Elghobashi, S. & Sirignano, W. A. 1995 Unsteady flow interactions between an advected cylindrical vortex tube and a spherical particle. *J. Fluid Mech.* **288**, 123–155.

Kim, I., Elghobashi, S. & Sirignano, W. A. 1997 Unsteady flow interactions between a pair of advected vortex tubes and a rigid sphere. *Intl J. Multiphase Flow* **23**, 1–23.

Kim, I., Elghobashi, S. & Sirignano, W. A. 1998 On the equation for spherical-particle motion: effect of Reynolds and acceleration numbers. *J. Fluid Mech.* **367**, 221–253.

Kulick, J. D., Fessler, J. R. & Eaton, J. K. 1993 On the interactions between particles and turbulence in a fully-developed channel flow in air. *Tech. Rep.* MD-66. Mechanical Engineering Department, Stanford University.

Kulick, J. D., Fessler, J. R. & Eaton, J. K. 1994 Particle response and turbulence modification in fully developed channel flow. *J. Fluid Mech.* **277**, 109–134.

Ladd, A. J. C. 1997 Sedimentation of homogeneous suspensions of non-Brownian spheres. *Phys. Fluids* **9**, 491–499.

Lee, M. J. 1985 Numerical experiments on the structure of homogeneous turbulence. PhD thesis, Stanford University.

Li, Y., McLaughlin, J. B., Kontomaris, K. & Portela, L. 2001 Numerical simulation of particle-laden turbulent channel flow. *Phys. Fluids* **13**, 2957–2967.

Lomholt, S., Stenum, B. & Maxey, M. R. 2002 Experimental verification of the force coupling method for particulate flows. *Intl J. Multiphase Flow* **28**, 225–246.

McLaughlin, J. B. 1991 Inertial migration of a small sphere in linear shear flows. *J. Fluid Mech.* **224**, 261–274.

Magnaudet, J., Rivero, M. & Fabre, J. 1995 Accelerated flows past a rigid sphere or a spherical bubble. Part 1. Steady straining flow. *J. Fluid Mech.* **284**, 97–135.

Mansour, N. N. & Wray, A. A. 1994 Decay of isotropic turbulence at low Reynolds number. *Phys. Fluids* **6**, 808–814.

Mavriplis, D. J. & Venkatakrishnan, V. 1995 Agglomeration multigrid for two-dimensional viscous flows. *Comput. Fluids* **24**, 553–570.

Maxey, M. R. & Patel, B. K. 2001 Localized force representations for particles sedimenting in Stokes flow. *Intl J. Multiphase Flow* **27**, 1603–1626.

Maxey, M. R., Patel, B. K., Chang, E. J. & Wang, L. P. 1997 Simulations of dispersed turbulent multiphase flow. *Fluid Dyn. Res.* **20**, 143–156.

Maxey, M. R. & Riley, J. J. 1983 Equation of a small rigid sphere in a nonuniform flow. *Phys. Fluids* **26**, 883–889.

Mei, R. 1994 Flow due to an oscillating sphere and an expression for unsteady drag on the sphere at finite Reynolds number. *J. Fluid Mech.* **270**, 133–174.

Mei, R. & Adrian, R. J. 1992 Flow past a sphere with an oscillation in the free-stream velocity and unsteady drag at finite Reynolds number. *J. Fluid Mech.* **237**, 323–341.

Mei, R., Lawrence, C. J. & Adrian, R. J. 1991 Unsteady drag on a sphere at finite Reynolds number with small fluctuations in the free-stream velocity. *J. Fluid Mech.* **233**, 613–631.

Michaelides, E. E. 2003 Hydrodynamic force and heat/mass transfer from particles, bubbles, and drops – The Freeman Scholar Lecture. *Trans. ASME J. Fluids Engng* **125**, 209–238.

Mittal, R. 2000 Response of the sphere wake to freestream fluctuations. *Theoret. Comput. Fluid Dyn.* **13**, 397–419.

Mohseni, K. & Colonius, T. 2000 Numerical treatment of polar coordinate singularities. *J. Comput. Phys.* **157**, 787–795.

Pan, T. W., Joseph, D. D., Bai, R., Glowinski, R. & Sarin, V. 2002 Fluidization of 1204 spheres: simulation and experiment. *J. Fluid Mech.* **451**, 169–191.

Pan, Y. & Banerjee, S. 1996 Numerical simulation of particle interactions with wall turbulence. *Phys. Fluids* **8**, 2733–2755.

Paris, A. D. & Eaton, J. K. 2001 Turbulence attenuation in a particle-laden channel flow. *Tech. Rep.* TSD-137. Mechanical Engineering Department, Stanford University.

Parthasarathy, R. N. & Chan, Y. H. 2001 Turbulence modification in dilute small-particle-laden liquid jets. *AIAA J.* **39**, 535–538.

Prosperetti, A. & Oğuz, H. N. 2001 Physalis: a new $o(N)$ method for the numerical simulation of disperse systems: potential flow of spheres. *J. Comput. Phys.* **167**, 196–216.

Rogers, C. B. & Eaton, J. K. 1991 The effect of small particles on fluid turbulence in a flat-plate, turbulent boundary layer in air. *Phys. Fluids* A **3**, 928–937.

Rouson, D. W. I., Eaton, J. K. & Abrahamson, S. D. 1997 A direct numerical simulation of a particle-laden turbulent channel flow. *Tech. Rep.* TSD-101. Mechanical Engineering Department, Stanford University.

Rubinow, S. I. & Keller, J. B. 1961 The transverse force on a spinning sphere moving in a viscous fluid. *J. Fluid Mech.* **11**, 447–459.

Ruge, J. W., Li, Y., McCormick, S., Brandt, A. & Bates, J. 2000 A nonlinear multigrid solver for a semi-Lagrangian potential vorticity-based shallow-water model on the sphere. *SIAM J. Sci. Comput.* **21**, 2381–2395.

Saffman, P. G. 1965 The lift on a small sphere in a slow shear flow. *J. Fluid Mech.* **22**, 385–400.

Sato, Y. & Hishida, K. 1996 Transport process of turbulence energy in particle-laden turbulent flow. *Intl J. Heat Fluid Flow* **17**, 202–210.

Squires, K. D. & Eaton, J. K. 1990*a* Particle response and turbulence modification in isotropic turbulence. *Phys. Fluids* A **2**, 1191–1203.

Squires, K. D. & Eaton, J. K. 1990*b* The interaction of particles with homogeneous turbulence. *Tech. Rep.* MD-55. Mechanical Engineering Department, Stanford University.

Sundaram, S. & Collins, L. R. 1999 A numerical study of the modulation of isotropic turbulence by suspended particles. *J. Fluid Mech.* **379**, 105–143.

Tennekes, H. & Lumley, J. L. 1974 *A First Course in Turbulence*. MIT Press, Cambridge, MA.

Tomboulides, A. G. & Orszag, S. A. 2000 Numerical investigation of transitional and weak turbulent flow past a sphere. *J. Fluid Mech.* **416**, 45–73.

Tsuji, Y., Morikawa, Y. & Shiomi, H. 1984 LDV measurements of an air–solid two-phase flow in a vertical pipe. *J. Fluid Mech.* **139**, 417–434.

Zhang, Z. & Prosperetti, A. 2003 A method for particle simulation. *Trans. ASME J. Appl. Mech.* **70**, 64–74.